Ambient Seismic Noise Tomography of Canada and Adjacent Regions: Part I Crustal Structures

Honn Kao[1,2*], Yannik Behr[3,4], Claire Currie[5], Roy Hyndman[1,2], John Townend[4], Fan-Chi Lin[6], Michael H. Ritzwoller[7], Shao-Ju Shan[1], and Jiangheng He[1]

[1] Geological Survey of Canada, Pacific Geoscience Centre, Sidney, BC, Canada

[2] School of Earth and Ocean Sciences, University of Victoria, Victoria, BC, Canada

[3] Swiss Seismological Service, ETH Zurich, Switzerland

[4] Institute of Geophysics, Victoria University of Wellington, Wellington, New Zealand

[5] Department of Physics, University of Alberta, Edmonton, Alberta, Canada

[6] Division of Geological and Planetary Sciences, California Institute of Technology, Pasadena, CA, United States

[7] Department of Physics, University of Colorado at Boulder, Boulder, CO, United States

* Corresponding Author, postal address: Geological Survey of Canada, Pacific Geoscience Centre, 9860 West Saanich Road, Sidney, B.C. V8L 4B2, Canada; phone: 1-250-363-6625; email: hkao@nrcan.gc.ca

(submitted to *JGR-SE,* July 16, 2013)

Abstract. This paper presents the first continental-scale study of the crust and upper mantle shear-velocity (V_s) structure of Canada and adjacent regions using ambient noise tomography. Continuous waveform data recorded between 2003 and 2009 with 788 broadband seismograph stations in Canada and adjacent regions are used in the analysis. The higher primary frequency band of the ambient noise provides better resolution of crustal structures than previous tomographic models based on earthquake waveforms. Prominent low-velocity anomalies are observed at shallow depths (<20 km) beneath the Gulf of St. Lawrence in east Canada, the sedimentary basins of west Canada, and the Cordillera. In contrast, the Canadian Shield exhibits high velocities. We characterize the crust–mantle transition in terms of not only its depth and velocity but also its sharpness, defined by the thickness of the transition and the amount of velocity increase. Considerable variations in the physical properties of the crust–mantle transition are observed across Canada. Positive correlations between the crustal thickness, Moho velocity, and the thickness of the transition are evident throughout most of the craton except near Hudson Bay where the uppermost mantle V_s is relatively low. Prominent vertical V_s gradients are observed in the mid-crust beneath the Cordillera and in the craton beneath most of the Canadian Shield. The mid-crust velocity contrast beneath the Cordillera may correspond to a detachment zone associated with high temperatures immediately beneath, whereas the large mid-crust velocity gradient beneath the Canadian Shield probably represents a rheological boundary between the upper and lower crust.

1. Introduction

The continental lithosphere of Canada contains a record of tectonic events that have shaped the region over the last 4 Gyr, from the ancient orogens that formed the cratonic core to on-going deformation of the more juvenile accreted terranes of the Canadian Cordillera. This area, which extends for >3000 km between the Atlantic and Pacific Oceans and a similar distance north–south (Figure 1), can be divided into three major geological domains: orogenic belts (the tectonically active

Cordillera in the west and the inactive Appalachian and Innuitian in the east and north, respectively); the central Archean shield; and the surrounding younger platforms (including sedimentary basins underlain by the Archean rocks) [e.g., *Fulton*, 1989; *Vincent*, 1989; *Wheeler et al.*, 1997]. Present-day tectonic activity occurs mainly in the west in the Cordillera, where subduction of the Juan de Fuca and Explorer plates beneath the North America plate takes places in the south and strike-slip motion between North America and the Pacific plate takes place further north (Figure 1). The last tectonic events on the east Appalachian and arctic Innuitian regions were the Taconic orogeny in the Early Paleozoic and the Eurekan orogeny in the Early Paleocene, respectively [*Okulitch and Trettin*, 1991; *Williams*, 1979]. The tectonic history thus varies dramatically from west to east and there are associated significant variations in lithospheric structure as explored in this study.

Both global and regional tomographic studies using earthquake sources have identified the systematic seismic velocity differences between the continent's cratonic center and the Cordillera and Cascadia subduction zone in the west [*Dalton et al.*, 2009; *Lebedev and van der Hilst*, 2008; *Lekic and Romanowicz*, 2011; *Mercier et al.*, 2009; *Simmons et al.*, 2010; *van der Lee and Frederiksen*, 2005; and references therein]. The lateral transition from high upper mantle velocities associated with the cold craton to lower velocities beneath the hot Cordillera is abrupt [e.g., *Hyndman and Lewis*, 1999], but geographically complex [e.g., *Bank et al.*, 2000; *Bensen et al.*, 2008; *Frederiksen et al.*, 1998; *Mercier et al.*, 2009; *van der Lee and Frederiksen*, 2005]. Similarly, variations in crustal thickness across the continent have been extensively documented, with average to thick (40–45 km) crust in the craton and other stable areas in the middle of the continent [e.g., *Cook et al.*, 2010; *Ma et al.*, 2012; *Mooney et al.*, 1998; *Perry et al.*, 2002] and thin (~35 km) crust beneath the Cordillera [*Clowes et al.*, 2005; *Mooney et al.*, 1998; *Perry et al.*, 2002]. There have been numerous studies addressing aspects of the seismic and thermal structures of various parts of the Canadian Shield [e.g., *Audet and Mareschal*, 2004; *Cheng et al.*, 2002; *Frederiksen et al.*, 2007; *Guillou-Frottier et al.*, 1996; *Mareschal et al.*, 2005; *Perry et al.*, 2006; *Shapiro et al.*, 2004b; and references therein] and the Cordillera [e.g., *Cassidy*, 1995; *Frederiksen et al.*, 1998; *Hyndman et al.*, 2005; *Mercier et al.*, 2009]. However, a detailed understanding of exactly how the transition in seismic velocity and crustal thickness from craton to Cordillera is accommodated requires a consistent and systematic approach spanning the entire region.

Ambient seismic noise tomography has recently become a well-established velocity mapping technique [e.g., *Behr et al.*, 2011; *Bensen et al.*, 2009; *Fulton*, 1989; *Ritzwoller et al.*, 2011; *Sabra et al.*, 2005; *Shapiro et al.*, 2005; *Tibuleac et al.*, 2011; *Wapenaar et al.*, 2008]. One of its advantages over traditional earthquake-based tomographic methods is its avoidance of heterogeneously distributed earthquake sources. Also, due to the high-frequency spectral content of the ambient noise used, this technique is particularly well suited to high-resolution imaging of velocity structures at crustal and uppermost mantle depths [*Behr et al.*, 2011; *Lin et al.*, 2008; *Lin et al.*, 2007]. Its recent widespread adoption has been promoted by the rapid expansion of global, regional, and local broadband seismograph networks. Efficient seismic data management and distribution, as well as increasing computational capacity, have also only recently made possible the processing of the large volumes of ambient seismic noise data involved.

By utilizing ambient noise records made throughout Canada and adjacent parts of the United States and Greenland (Figure 2), the goal of this study is to establish the crust and upper mantle velocity structure at a resolution as high as the local and regional data permit and to investigate all the geological provinces with the same methodology and processing procedures. Based on the surface wave tomographic results obtained, we then estimate the 3D shear-velocity (V_s) distributions to upper mantle depths. We focus mainly on crustal and uppermost mantle structures with special emphasis on the topography and character of the Moho discontinuity. Finally, we address how abruptly the crustal velocity and thickness vary among the geological provinces and discuss the tectonic implications of these variations.

2. Data and Analysis

In this section, we first describe the ambient noise data used in our analysis, followed by an introduction to the data processing procedures, tomographic inversion, and the conversion of surface wave results obtained at different periods to 3D shear-wave velocities.

2.1. Ambient Seismic Noise Data

Continuous digital broadband seismic waveforms recorded by the Canadian National Seismograph Network (CNSN) and the Portable Observatories for Lithospheric Analysis and Research Investigating Seismicity (POLARIS) between 2003 and 2009 constitute the core component of our data set. To provide velocity resolution near the boundaries of the main study area, we also make use of broadband waveforms from stations north of 40°N within the United States, mainly from the United States Advanced National Seismic System and the dense temporary United States Transportable Array (USArray), east of 150°W in Alaska (mainly the Alaska Regional Seismic Network), and along the western coastline of Greenland (included as part of the Global Seismic Network). We further include stations of the Canadian High Arctic Seismic Monitoring Experiment (CHAME) to provide critical data coverage for the arctic north. Figure 2 shows the station distribution of our dataset and the corresponding ray path coverage.

CNSN, POLARIS and CHAME waveform archives were obtained from the CNSN Data Center, whereas the other data were obtained from the Data Management Center of the Incorporated Research Institutions for Seismology (IRIS). The combined dataset includes records from 843 stations covering a time window of 2557 days. Because not all stations operated at the same time, especially those of the USArray, it is not possible to have a complete combination of all station pairs for any given day. On average, our dataset has half to two thirds of the stations represented on any one day.

2.2. Seismic Waveform Processing

We follow the procedures outlined by *Bensen et al.* [2007] to process the waveform data. For each station, the vertical component waveforms are first split into one-day segments, followed by the subtraction of the amplitude mean and trend, removal of the instrument response, time-domain normalization using the running-absolute-mean method, and spectral whitening. Cross correlation functions (CCFs) are calculated for the daily waveforms for each station pair. We employ a two-stage stacking scheme, first monthly then total, to accommodate the large volume of data. On average, each station yields more than 12,000 monthly CCFs. For some long-running stations, the number of CCFs exceeds 25,000.

Figure 3 shows four representative examples from CNSN stations with the final stacked CCF. Because of the large number of samples, we plot only the trace with the highest signal-to-noise (S/N) ratio for each 100 km distance interval. For the two stations on the east and west coasts (LMN and PGC, respectively; Figures 3a and b), the Rayleigh wave move-out can be clearly observed across the continent to offsets of more than 5000 km. For the stations located in the northwest (INK) and southeast (ACTO), the move-out spans more than 4000 km (Figures 3c and d). All four stations show pronounced differences between the causal (positive) and acausal (negative) branches of the CCF, which are most likely due to azimuthally biased noise source distributions [e.g., *Stehly et al.*, 2006].

2.3. Dispersion Measurement

The positive and negative branches of the correlation function are averaged to give the symmetric component, which is used thereafter to estimate the Rayleigh wave dispersion curves [*Bensen et al.*, 2007]. The commonly used frequency–time analysis (FTAN) with phase-matched filtering [*Levshin and Ritzwoller*, 2001] is applied to track the dispersion ridge from the spectral image and to minimize the effects of spurious noise glitches or jumps in group arrival times. The corresponding phase velocities are obtained using the approach described by *Lin et al.* [2008].

For each station pair, we conduct the phase-matched filtering FTAN for the period range of 5–250 s.

If the analysis results in no output, due to the abrupt discontinuity in the dispersion measurements, we incrementally decrease the maximum period (from 250 s to 200, 150, 100, 75, or 50 s) to maintain both the quantity and quality of our input data.

In Figure 4, we show the stacked symmetric CCFs and the corresponding dispersion curves for two representative station pairs spanning the western (PGC–FFC, station distance 1625 km) and eastern (DRLN–FFC, station distance 3064 km) halves of the Canadian continent, respectively (station locations shown in Figure 2). The dispersive characteristics of Rayleigh waves can be clearly recognized on traces derived from stacking only one year of ambient noise data (top traces, Figure 4). As the duration of the data used in the stacking increases from one to three years, the S/N ratios improve accordingly (middle traces, Figure 4). However, the S/N improvement becomes much less significant when we increase the stacking dataset from three to seven years (bottom traces, Figure 4), suggesting that the benefit of including data beyond 2009 is probably limited for present purposes.

As our dataset covers all the northern states of the US in which ambient noise tomography has been undertaken previously [*Bensen et al.*, 2008; *Bensen et al.*, 2009; *Shen et al.*, 2013], it is important to ensure that the stacked CCFs and dispersion measurements derived in this study are consistent with those reported from earlier studies. For this purpose, we compare our results with the stacked CCFs available from the Data Management Center of IRIS (IRIS DMS Product, Western US Ambient Noise Cross-Correlations, by Mikhail Barmine and Michael Rtizwoller, published electronically June 2012, Incorporated Research Institutions for Seismology, Last accessed March 26, 2013, http://www.iris.edu/dms/products/ancc-ciei). A representative example is shown in Figure 5 (RLMT and NLWA; locations shown in Figure 2). Although the datasets used in the two studies span different years, all the waveform characteristics in the stacked CCF are remarkably similar. The dispersion measurements are essentially identical except at the longest periods (>90 s) where the difference is about 0.2 km/s due to the deterioration of data resolution. This provides us with confidence in both the dataset and analysis employed in this study.

2.4. Surface Wave Tomography Inversion

We use the method of *Barmin et al.* [2001] to derive tomographic images from Rayleigh wave dispersion data. For each period, the inversion estimates the 2D distribution of group and phase velocity perturbations across a spherical grid of 1° spacing in a damped least-squares sense. The damping is controlled by two parameters specifying the weight of smoothing and the width of the smoothing area. We take an empirical approach to determine the optimal combination of the two weighting parameters, by systematically examining the mean and standard deviation of the overall misfit function of the inversion. The parameters corresponding to the least damping with a mean misfit close to zero and a small standard deviation are adopted in deriving our final velocity results which is shown in Figure 6. A more detailed discussion of our tomographic inversion results will be given in the next section.

Several previous studies have argued that the tomographic resolution inferred from the commonly used checkerboard test may be misleading [e.g., *Leveque et al.*, 1993] or difficult to interpret [e.g., *Simons et al.*, 2002]. In this study, we choose the spike-perturbation test, as outlined by *Barmin et al.* [2001], to assess the resolution of our results. Specifically, we place a spike-like perturbation at a given node of the inversion grid and then examine the corresponding inversion output. The spatial resolution at that node is defined by the minimum distance at which a neighboring spike can be unambiguously identified. As expected, we find that the spatial resolution is closely linked to the density of local stations and the number of ray paths.

2.5. Conversion From Surface Wave Tomography to 3D Grid Tomography

To convert the set of surface wave maps at successive periods into a 3D shear-velocity model, we employ the method of *Shapiro et al.* [2004a] as implemented by *Behr et al.* [2010; 2011]. At each 1° grid point, a new dispersion curve is computed by interpolating between the values at successive periods. Each newly derived dispersion curve is then inverted for a 1D shear-velocity profile using the Neighbourhood Algorithm (NA) [*Sambridge*, 1999a; *Sambridge*, 1999b], resulting in 4949 shear velocity–depth profiles. The NA is a direct search method, similar to the Monte-Carlo algorithm or simulated annealing, which solves optimization problems by exploring the range of possible solutions in a quasi-random manner. It returns best-fitting models and an estimate of the distribution of models in the parameter space as a function of their misfit. For each 1D shear-velocity model, the misfit is computed as the least-squares difference between the dispersion curve of the model and the one constructed from the surface-wave maps. This approach enables us to evaluate the resolution and the level of ambiguity of each best-fitting shear-velocity model. We employ the software package Dinver (www.geopsy.org) [*Wathelet*, 2008] which combines the forward modeling algorithm of *Dunkin* [1965] with an improved version of the original NA. The current version of the Dinver algorithm does not allow for parameterization of a top water layer, and therefore areas of shallow waters (e.g., lakes or bays) are given a top layer of extremely low shear strength. Inversions for areas with a thick water column, such as the Pacific and Atlantic oceans, are disregarded in our analysis.

One hundred new models and their misfits are computed for each of the 300 NA iterations, resulting in 30,000 shear-velocity models being evaluated at each grid point. We follow the scheme of CRUST2.0 to parameterize the crustal portion of each model as a stack of five homogeneous, isotropic layers corresponding to sediments, sedimentary basement, upper crust, middle crust and lower crust. One or two mantle layers are setup to extend the model to upper mantle depths. We assume that the shear modulus is independent of frequency (i.e., shear Q is essentially infinite). This significantly simplified the forward calculation and can be justified on the ground that our study focus is the crust where the Q tends to be larger than that in the mantle. Another justification is that much of the region of study is stable craton with large Q values. Although the top layer of sediments may have relatively low Q, its effect is generally negligible in our case due to its thin thickness (0 to a few km).

Each layer is characterized by thickness, compressional velocity (V_p), shear velocity (V_s) and density. The NA varies the thickness, V_p and V_s but not density for each layer at each iteration and computes the misfit. Density has been shown to have only minor influence on the resulting dispersion curve [*Wathelet*, 2005] and has therefore been kept constant at the values of CRUST2.0 in the crust and PREM in the mantle.

To obtain a stable (reproducible) result, it is necessary to impose some constraints on the parameter space. We achieve this by incorporating *a priori* knowledge of the shear-velocity profile at a particular grid point. For the crust, we allow the NA to vary each inverted parameter by 20% around the CRUST2.0 model [*Bassin et al.*, 2000]. The crustal thickness is taken from the LITH5.0 model [*Perry et al.*, 2002], where available, and from CRUST2.0 otherwise. Values for the mantle layers are taken from the PREM model [*Dziewonski and Anderson*, 1981] and we again allow the parameters to vary by 20%.

We conduct forward modeling to estimate the uncertainty in the inversion results. For each best-fitting model, we systematically perturb each inverted parameter and calculate the root-mean-square (RMS) error between observed and synthetic dispersion curves. Because the overall fit to the phase velocity dispersion curve is 2–3 times better than the fit to the group velocity [*Lin et al.*, 2008], we adjust the relative weighting between the two by a factor of 2.5 to prevent the uncertainty estimate being dominated by the group velocity misfit. The parameter's range of uncertainty is set at the values corresponding to a 5% RMS increase.

At each grid point, we calculate the weighted average of the top 5% best-fitting model samples using the inverse of the misfit value as the weighting factor. These weighted best-fitting 1D models are then combined and linearly interpolated laterally to form the final pseudo-3D model. The weighted average approach is a practical and perhaps better alternative to choosing the best-fitting model, especially when multiple model samples have almost the same misfit values.

In Figure 7, we show representative examples of the NA inversion results for points in four different tectonic settings: the Cordillera, the Interior Platform, the Canadian Shield, and the Appalachian (see Figures 1 and 9c for locations). The surface-wave dispersion curves are clearly different from one node to another. One important feature in the group velocity dispersion curves is the broad trough in the 15–30 s period range that effectively constrains the depth of the crust–mantle transition [*Lebedev et al.*, 2013]. The trough is the narrowest and shifted toward shorter periods in the Cordillera, where the Moho is relatively shallow (Figure 7a). A broader trough is observed inside the craton where the crust is thicker (Figures 7b and c). In comparison, the broadness of the trough is intermediate in the Appalachian where the Moho depth is in between those of the Cordillera and the craton (Figure 7d).

The robustness of the inversions is well illustrated by the concentration of best-fitting models in a relatively narrow portion of the model space (Figure 7). For nearly all the NA inversions that we have performed, the results are robust and can be reproduced with different sets of starting models. Figure 8 shows the distribution of best-model misfits. Overall, better results are obtained for the Canadian Shield and the Appalachian regions (misfit <0.07 km/s) than for the Cordillera and the Interior Platform (<0.15 km/s).

3. Seismic Inversion Results

In this section, we first present the surface-wave tomography results and then the pseudo-3D shear-velocity results computed from ambient seismic noise CCFs. We emphasize the variation of crustal structures, including the depth and velocity characteristics of the Moho. The dominant frequencies of ambient seismic noise are well suited to study such depths, in contrast to those of most earthquake tomographic studies that focus on lower frequencies and correspondingly greater depths.

3.1. Surface Wave Tomography–General Features

Since the vertical component waveforms are used in our ambient seismic noise analysis, our surface wave tomography corresponds to the distribution of group and phase velocities of Rayleigh waves. In Figure 6, we show the velocity distributions, horizontal resolution, and depth sensitivity for three periods (10, 35, and 50 s), which are most sensitive to the depth ranges of 5–15 km, 15–50 km, and 30–80 km, respectively. The horizontal resolution corresponds to one standard deviation of the best-fitting Gaussian surface at each point [*Lin et al.*, 2007].

In general, group and phase velocity distributions are similar at all periods. At shorter periods (e.g., 10 s, Figure 6a), velocity anomalies are dominated by large-scale sedimentary basins and upper crust structures. Prominent low-velocity anomalies are observed for the Gulf of St. Lawrence Basin in the east, the sedimentary basins of west Canada, and in the Cordillera. In contrast, the Canadian Shield exhibits high velocities.

The low-velocity signature beneath the Gulf of St. Lawrence disappears at periods larger than 35 s. Similarly, the low-velocity anomalies associated with the Cordillera are much less visible. Overall, the velocity contrast between high and low anomalies is smaller, and the high velocities associated with the craton expand slightly toward the west under the western Canadian sedimentary basin (i.e., the Interior Platform (Figures 1 and 6b). Such a westward expansion of the high-velocity anomaly is even more prominent at longer periods (e.g., 50 s, Figure 6c).

Generally speaking, our data provide reasonable constraints on Rayleigh-wave velocities to latitudes of ~70°N. Further north, the station distribution becomes sparse and the image resolution deteriorates. Taking the 10 s period as an example, the large volume of data results in a horizontal resolution of 150 km or less for most grid points south of 70°N. The spatial resolution also deteriorates with increasing period as the number of useful CCFs decreases. The image deterioration becomes progressively worse for the northern region.

3.2. Pseudo-3D Grid Tomography

We invert for the shear-velocity (V_s) distribution across the study region at 1° intervals. In Figure 9, we show the pseudo-3D tomographic images at three depths corresponding to the top sedimentary layer and upper crust (5 km), the lower crust (25 km), and the uppermost mantle (50 km). E–W and N–S vertical cross sections are shown in Figure 10.

At the 5 km depth, there are a number of prominent low-V_s anomalies. The most pronounced are on the western side of the continent, including the Cascadia forearc (the Georgia-Pudget-Wallamette basin of southwestern British Columbia, western Washington, and central-western Oregon), the Rocky Mountains (eastern Idaho, western Montana and Wyoming), and the Canadian Cordillera (Figures 1 and 9). The low- V_s anomalies in the northern US have been documented previously using the same tomography technique [*Bensen et al.*, 2009; *Shen et al.*, 2013]. The low-V_s signature of the Cordillera and Cascadia forearc remains visible down to the uppermost mantle. This is particularly evident when comparing the profile through the Canadian Cordillera to the one through the western Canadian Shield (Profiles 1–1' vs. 2–2', Figure 10). We also find that the shallow low velocities beneath the Cordillera extend north to the Yukon and Northwest territories (Figure 9).

For east Canada, the V_s patterns are similar between the western and the eastern parts of the Canadian Shield, as shown by Profiles 2–2' and 3–3' in Figure 10, respectively. The most obvious shallow low-V_s anomaly is located beneath the southern Gulf of St. Lawrence sedimentary basin. Another low-V_s anomaly is found beneath Lake Superior where an ancient mid-continental rift system is inferred from geological and geophysical data [*Cannon et al.*, 1989]. However, there is no evidence of thick sediments because the rift system went through a stage of tectonic inversion 1.1 b.y. ago with the central graben being uplifted by at least 5 km [*Cannon et al.*, 1989]. Consequently, we suspect that the observed low-V_s anomaly beneath Lake Superior is not a manifestation of a thick sedimentary basin. Instead, it might be an artifact due to the leaking effect from the top water layer.

From the three E–W profiles (A–A', B–B', and C–C' in Figure 10), it is clear that the highest V_s at the uppermost mantle depths is not directly associated with the center of the Canadian Shield. Instead, the highest V_s corresponds to the stable Interior Platform and the outer rim of the Canadian Shield (900–1400 km in Profile A–A', 650–2050 km in Profile B–B', and 1000–2500 and 3250–3900 km in Profile C–C'). In general, the inner part of the Shield appears to have V_s consistently lower than that of the outer rim for all of the mantle depths resolvable by our data.

There are two interesting features in Profile C–C' that are distinct from the other profiles. One is the dome-like high-V_s anomaly in the mid- and lower crust between ~20 and 40-km depths just to the west of Profile 2–2' (the region centered at the US-Canada border between Montana and Manitoba, Figure 9b). The other is the generally broader vertical transition between lower crust and uppermost mantle, a feature we discuss in some detail in the next section.

3.3. Crust–mantle Transition

The crust–mantle transition ("Moho") was first discovered in Europe as a subsurface velocity interface across which V_p rapidly increases from ~5.6 to >7.75 km/s and V_s from 3.27 to 4.18 km/s [*Mohorovicic*, 1910]. Early studies concluded that the Moho generally corresponded to the depth at which the density of earth materials increases dramatically due to either compositional or phase changes [e.g., *Adams and Williamson*, 1923; *Green and Ringwood*, 1972; *Ito and Kennedy*, 1971]. However, as refraction seismology was undertaken in different part of the world, geophysicists realized that substantial variations exist in the Moho discontinuity's depth distribution, the magnitude of the velocity contrast, and its vertical dimension [e.g., *Cook et al.*, 2010; *Mooney*, 1987]. Furthermore, different remote sensing techniques (seismic refraction, seismic reflection, magnetotelluric measurements, etc.) often yield different Moho depths that may correspond to different physical aspects of the crust–mantle transition [e.g., *Catchings and Mooney*, 1991; *Cook et al.*, 2010; *Mooney and Brocher*, 1987]. Consequently, an appropriate modifier is usually placed in front of the term "Moho" (such as refraction Moho, reflection Moho, or electric Moho) to indicate the specific geophysical technique employed in the survey [e.g., *Cook et al.*, 2010].

Globally, the Moho discontinuity is recognized as a large velocity increase from V_p~6.8–7.3 km/s to V_p~8.2 km/s [e.g., *Mooney et al.*, 1998]. Using a typical V_p–V_s relationship derived from laboratory data [*Christensen*, 1996], the corresponding V_s jump is estimated to be 0.42–0.82 km/s (from V_s of 3.73–4.13 to 4.55 km/s). In Figure 10, we mark the two depths at which the V_s has increased from a typical crustal velocity to a typical upper mantle velocity by 50% and 85% with the blue and red lines, respectively. The schematic diagram in Figure 11 illustrates how these two depths are determined. Specifically for each grid point, we first identify the lower crust shear velocity ($V_{s,crust}$) and the uppermost mantle velocity ($V_{s,mantle}$) from the corresponding V_s profile. The V_s increased at a given level is defined as

$$V_r = V_{s,crust} + r\,(V_{s,crust} - V_{s,mantle}) \qquad (1)$$

where r is the percentage of V_s increase (e.g., 50% or 85%).

In Figure 12, the depth range corresponding to this 50%–85% V_s increase, hereafter referred to as $dZ_{50\%\text{-}85\%}$, is colored in gray. Most of the large velocity gradients occur where V_s jumps from ≤3.8 km/s to ≥4.2 km/s (Figure 10). However, there are exceptions where the downward velocity increase is gradual rather than abrupt. Given the varying thickness of the velocity increase from crust to uppermost mantle, the depth of a specific V_s or an abrupt velocity jump (which is the common definition of a "refraction Moho," [e.g., *Steinhart*, 1967]) cannot fully characterize the crust–mantle transition. Similarly, the reflection Moho and electric Moho, which have been defined as "the deepest, high-amplitude, laterally extensive reflection or group of reflections" and "a step change in electrical conductivity" present in the vicinity of the corresponding refraction Moho, respectively [e.g., *Cook et al.*, 2010; *Jones and Ferguson*, 2001; *Klemperer et al.*, 1986], cannot well serve the purpose in some areas either.

The appropriate definition of the "Moho" depends on the application. While the ambient seismic noise dispersion measurement is not the ideal tool to pinpoint the location of a seismic reflector such as the Moho, it is capable of distinguishing a sharp velocity discontinuity from a gradual one. This unique advantage enables us to examine the crust–mantle transition from a different perspective. For places where the V_s increase is gradual, a gradational transition between crustal and mantle compositions is implied. It is not yet possible to determine whether the gradational layer is an intercalated mixture of crustal and mantle rocks or another mixed structure.

As a general measure appropriate for many applications, including isostasy calculations, we propose a more comprehensive method of characterizing the crust–mantle transition. In Figure 13, the depth contours corresponding to V_s increase 50% and 85% from lower crust to uppermost mantle are plotted along with the corresponding velocities, $V_{50\%}$ and $V_{85\%}$, and their differences. Although it is convenient to identify the depth contour of $V_{85\%}$ (i.e., $Z_{85\%}$) as a proxy for the "ambient noise" Moho, it is important to realize that the abruptness of the crust–mantle transition is clearly not uniform across the continent. Most areas beneath which a relatively sharp Moho discontinuity, i.e., $dZ_{50\%\text{-}85\%}$ <2 km, is inferred beneath the Canadian Shield (Figure 13c). For other regions, using a single Moho depth to define the crust–mantle transition is probably inappropriate.

To first order, the depth distribution of the 85% crust–mantle V_s increase (i.e., $Z_{85\%}$, Figure 13a) is similar to that presented by *Bensen et al.* [2009] and *Cook et al.* [2010] for regions south and north of the Canada–US border, respectively. Relatively thick crust is found surrounding the Canadian Shield, whereas thin crust is associated with active deformation such as the Cordillera and Cascadia. Overall, the crustal thickness beneath most of the Canadian craton is in the range of 35–41 km.

The Moho V_s, as represented by $V_{50\%}$ and $V_{85\%}$, shows a clear difference between the Cordillera and the continental interior (Figures 13d and 13e). Relatively low $V_{85\%}$ (i.e., ≤4.1 km/s) is observed beneath the entire western orogenic belt including the Canadian Cordillera, the Columbia Plateau, and the Cascadia forearc. In contrast, most of the Canadian craton and central US (e.g., northern Central Lowlands and Great Plains) are associated with relatively high Moho V_s. One exception is the central

Hudson Bay Platform where the corresponding $V_{85\%}$ is obviously lower. The relatively low crustal velocity beneath the Hudson Bay was also documented in a previous study using a regional dataset of ambient seismic noise [*Pawlak et al.*, 2010].

For the cratonic region, an overall correlation amongst crustal thickness, Moho V_s, and the thickness of the crust–mantle transition can be recognized (Figure 13). As the crust thickens from the center of the Canadian Shield outward, the corresponding $V_{85\%}$ and $dZ_{50\%\text{-}85\%}$ increase as well, except near Hudson Bay where the $V_{85\%}$ appears to be the lowest. Such correlation does not seem to hold for the Cordillera, either. While the Cordillera has a thinner crust and a lower $V_{85\%}$ than the craton, the thickness of the crust–mantle transition is in the middle range varying between 2 and 5 km.

3.4. Large Velocity Gradients in Mid-Crust

Our tomographic results show the existence of large vertical V_s gradients within the mid-crust in some areas. Examples of these large mid-crust gradients can be recognized from the six cross sections across different parts of the continent in Figure 10 and the V_s profiles shown in Figure 14. Their geographic distribution, however, is not uniform across Canada, and their depth distribution varies from one region to another. In most cases, the V_s increase is between 0.2 and 0.5 km/s.

The most prominent mid-crust V_s gradient is observed beneath the Cordillera, best shown in the Profile 1–1' of Figure 10. Its depth appears to increase to the south. The section just south of Profile A–A' has a large mid-crust V_s gradient at ~5 km depth. It is located at ~9 and 11 km beneath the sections around the Profile B–B' and to the south of C–C', respectively. In addition, the large mid-crust V_s gradient is not continuous across the entire Cordillera. Several gaps, each a few hundreds of km long, exist between sections where the large mid-crust V_s gradient is clear.

Another region in which a prominent mid-crust V_s gradient is observed is the craton beneath part of the Canadian Shield. The western half of the Superior Province (between 2300 and 3100 km in the Profile C–C', Figure 10; also the profiles GL-A and GL-C, Figure 14) shows a clear V_s jump at the depth of ~12 km. This large V_s jump defines the lower boundary of the upper crust.

A large mid-crust V_s gradient also exists beneath the easternmost section of Profile B–B' where the Canadian Shield meets the Appalachian belt (Figure 10). However, it is not common in the Appalachians because similar V_s jumps are not observed beneath the easternmost end of the Profile C–C'. Unfortunately, limited data resolution prevents us from obtaining a high-resolution velocity image for this part of the continent. Future investigation with a denser regional seismograph network in the region is needed.

4. Quantitative Comparison with Previous Models

In this section, we make quantitative comparisons of our results with previous models in the literature that were derived from different datasets. By systematically examining and characterizing both the similarity and difference, the purpose is to provide an objective assessment of our model in terms of regional variation and data resolution.

4.1. Lithoprobe Transects

In Figure 14, we show ten selected V_s profiles from our results and compare them with nearby seismic reflection profiles from the Lithoprobe program [*Clowes et al.*, 1984; *Cook*, 2002]. The map locations of the ten V_s profiles are marked in Figure 9c as red crosses. These examples are chosen because either they show a gradual crust–mantle transition or the location of the largest velocity gradient is inconsistent with the previously reported Moho depths. Specifically, we compare five V_s profiles in the vicinity of Profile B–B' with Lithoprobe transects AB-CAT1 (at a distance of ~1200 km; Figure 10), THOT-S1a (~1500 km), WS-2a (~2300 km), WS-1a (~2600 km), and another five V_s profiles in the vicinity of Profile C–C' with transects GL-C (~2400 km) and GL-A (~2700 km).

The base of common deep crustal sub-horizontal reflectivity usually is close to the defined Moho but there are some exceptions. For the transect AB-CAT1 passing through the Interior Platform in central Alberta, the bottom part of the zone containing strong seismic reflectors was used in previous studies to define the "reflection" Moho at a depth of 40 km [*Perry et al.*, 2002]. In our results, it corresponds to a velocity increase over a 7-km range between 33 km and 40 km (V_s profiles at 54°N, 115°W and 53°N, 115°W, Figure 14). Similar situations are observed for transect THOT-S1a through the Western Canadian Sedimentary Basin (55°N, 107°W) and transect WS-2a through the western part of the Superior Craton (50°N, 95°W), except that the Moho discontinuity in the LITH5.0 model is ~4 km deeper. Near the northern end of transect WS-1a in the central Superior Craton (52°N, 90°W), the discrepancy among our V_s profile, the seismic reflection image, and the LITH5.0 model is apparent as the bottom of the strong seismic reflector zone (i.e., the reflection Moho) is located between the largest velocity gradient at 32–38 km and the Moho depth in the LITH5.0 model (i.e., the refraction Moho) at 43 km.

One of the biggest inconsistencies between the crust–mantle velocity gradients found in our analysis and the Moho depths in the LITH5.0 model is observed in the vicinity of Lake Superior, where transects GL-A and GL-C are located. Taking transect GL-C as an example, the V_s profile near the northwestern end (48°N, 91°W) show a large velocity gradient between 36 and 41 km near the bottom of the zone of strong seismic reflectors. In comparison, the Moho depth is reported at 49 km in the LITH5.0 model, below which another gradual V_s increase is observed. Similarly, the V_s profile near the southeastern end of the transect GL-C (47°N, 89°W) exhibits a big velocity jump at 38–43 km that approximately coincides with the bottom of the strong seismic reflectors (Figure 14). A much smaller velocity increase is found at ~54 km depth where the LITH5.0 model defines the Moho discontinuity, although evidence from the seismic reflection image is unclear.

For the three locations near transect GL-A that passes through the center of Lake Superior (49°N, 87°W; 48°N, 87°W; 46°N, 88°W), the largest velocity gradients all correspond to strong seismic reflectors within rather than at the bottom of the reflector zones. Our V_s profiles show that the velocity begins to increase gradually at the depths where strong seismic reflectors become apparent, and the increase extends down to the bottom of the reflector zone where the Moho depth is defined in the LITH5.0 model.

4.2. “Ambient Noise” Moho vs. “Reflection” and “Refraction” Moho

In a global review of seismic reflection/refraction studies of the continental lithosphere, *Mooney and Brocher* [1987] pointed out that the lower crust appears to consist of laminated high- and low-velocity layers with typical thicknesses of 100–200 m, making it much more reflective than either the upper crust or the uppermost mantle. Therefore, the Moho depth determined from seismic reflection data may involve a clear reflector, but often is defined as the bottom of the reflective layers that generally coincides with the refraction Moho to within a few kilometers. For places with complex lower crustal and/or uppermost mantle structures, however, constructive and destructive interferences among seismic signals from different structures may lead to ambiguous interpretations of the Moho depths [e.g., *Catchings and Mooney*, 1991; *Cook*, 2002]. The occasionally significant discrepancies are well documented in the results of the Lithoprobe project in which the refraction and reflection Moho depths can differ by as much as 10 km [*Cook et al.*, 2010].

While the reflection and refraction Mohos are determined from V_p and P-wave impedance contrast, the "ambient-noise" Moho is based on the V_s distribution. Shear and compressional wave interface depths are expected to be similar but there is a possibility of differences. A direct comparison between the “ambient-noise” Moho relief determined in this study (Figures 12 and 13) and the Moho relief inferred from Lithoprobe reflection and refraction data (Figures 2 and 3 of *Cook et al.* [2010]) suggests that all three tend to agree that thin and thick crust is located beneath the Cordillera and craton, respectively. However, for a large portion of the cratonic region, the refraction Moho usually is the deepest, followed by the reflection Moho, and the ambient-noise Moho usually is the shallowest. The difference is generally <5 km. When a significant discrepancy exists between the reflection and refraction Moho, we notice that the ambient-noise Moho tends to be more consistent with the one that is better constrained. For example, the local variation in the ambient-noise Moho depth beneath central-northern Alberta (Figures 13a and 13b) is visible on the refraction Moho, as constrained by several Lithoprobe refraction transects, but not clear on the reflection Moho [*Cook et al.*, 2010]. Similarly, the locally shallower ambient-noise Moho beneath the Ontario–Quebec border is more consistent with the reflection Moho with constraints from a number of reflection profiles but not with the refraction Moho.

There are exceptions where the three Moho depths do not necessarily follow the downward order of ambient-noise, reflection, then refraction. One such example is observed in central Quebec (e.g., 53°N, 74°W) where the ambient-noise Moho is the shallowest ($Z_{50\%}$ and $Z_{85\%}$ at 32 and 36 km, respectively, Figure 13) followed by the refraction Moho (~39 km) and the reflection Moho (~45 km). Another similar example is in southern Quebec near the Canada–US border (e.g., 45°N, 73°W). Once again, the ambient-noise Moho is the shallowest ($Z_{50\%}$ and $Z_{85\%}$ at 35 and 38 km, respectively), followed by the refraction Moho at ~42 km and the reflection Moho at ~45 km. Notice that the numbers of available Lithoprobe transects, refraction or reflection, for both regions are very few, meaning that the inferred reflection or refraction Moho depths are less constrained.

It will need more detailed local studies to thoroughly investigate the relationships among different Moho depths and their physical relevance to the crust–mantle transition. In this paper, we provide only an initial discussion on this subject. In theory, different approaches are sensitive to different aspects of the velocity structure. While seismic reflection is best at illuminating velocity interfaces with large impedance contrast, seismic refraction is generally sensitive to the variation of velocity at depth. The difference may result in the refraction Moho being systematically deeper than the reflection Moho, especially if the bottom of the lower crust is not strongly reflective [*Catchings and Mooney*, 1991]. Since we define the ambient-noise Moho based on the sharpness of V_s variation across the crust–mantle transition, our result is expected to be more sensitive to the overall composition change than just the impedance contrast or the velocity of the bottom layer of the lower crust.

A recent study on the physical properties of the Paleozoic Cabo Ortegal Complex of NW Spain suggests that the crust–mantle transition is a gradation from felsic gneisses to ultramafic rocks with eclogites and mafic granulties in between [*Brown et al.*, 2009]. In such a scenario, the velocity Moho (reflection or refraction) actually corresponds to the boundary between the gneisses and the eclogite at a shallower depth, whereas the petrological Moho is located between the mafic granulites and ultramafic peridotites at a deeper depth. The fact that the ambient-noise Moho is often located shallower than the reflection or refraction Moho seems to imply that the deepest structure of the crust–mantle transition does not necessarily correspond to the largest velocity jump. It may be that the top of our Moho gradient layer marks the beginning of the gneisses–eclogite transition and the base represents the downward transition to ultramafic peridotite.

4.3. Previous Crustal and Tomography Models

Given the large number of previous studies of the seismic velocity structures of North America, it is impractical to compare our results with all the models described in the literature. There are also important issues to be considered before a meaningful comparison can be conducted, including the availability of model parameters, the scale and geographic coverage of each model, and the model resolution. However, to facilitate quantitative comparison of our model with any model of readers' interest, we have compiled a digital version of Figure 13 listing the physical parameters of the inferred "ambient noise" Moho and an ASCII table showing our tomography results (available online as electronic supplements). For demonstration purposes, we conduct comparisons with two crustal models cited frequently in this paper, CRUST2.0 [*Bassin et al.*, 2000] and LITH5.0 [*Perry et al.*, 2002], and two recent North American tomography models, NA04 [*van der Lee and Frederiksen*, 2005] and NA07 [*Bedle and van der Lee*, 2009], that are available in digital form at the IRIS website.

In Figure 12, we plot the Moho depths of the LITH5.0 [*Perry et al.*, 2002] and CRUST2.0 [*Bassin et *al.*, 2000] models as dashed blue and red lines, respectively, to summarize previous observations. Depending on the percentage of V_s increase defined in equation (1), the average depth difference between our model and the two previous crustal models may vary from -4.4 km ($Z_{50\%}$ - *CRUST2.0*) to 6.5 km ($Z_{100\%}$ - *LITH5.0*), as shown by the histograms in Figure 15.

Taking the $Z_{85\%}$ as a proxy for the "ambient noise" Moho, our result is on average 0.6 km shallower than that of CRUST2.0 model. This difference is negligible given the model uncertainty in our inversion. The corresponding standard deviation is 5.8 km. With respect to the LITH5.0 model, our model is on average 0.9 km deeper with a slightly larger standard deviation of 6.2 km. We notice that much of the high standard deviations stems from nodes where the discrepancy between the CRUST2.0 and LITH5.0 models exceeds 10 km. In other words, we will inevitably encounter a large discrepancy with respect to one or other of the two models at these nodes. We list the corresponding Moho depths of the CRUST2.0 and LITH5.0 models in the electronic supplement for the convenience of readers interested in comparing specific nodes/regions.

Both NA04 and NA07 models provide seismic velocity distribution for the entire upper mantle from 70 km to 670 km at interval of 20 km, whereas our tomography results only have adequate resolution for shallow depths (<100 km). Therefore, only the top two layers of the NA04 and NA07 models (i.e., 70 km and 90 km) are used in the comparison.

At a depth of 70 km, our model is on average 0.21 and 0.24 km/s slower than NA04 and NA07 models, respectively (Figure 16). The corresponding standard deviation of the velocity difference is 0.16 km/s for both. Most of the nodes with large discrepancies (i.e., larger than one standard deviation) are located near the boundary of our model where the ray path coverage is not optimal. However, there are places where the difference is large and yet the resolution length is reasonable (e.g., central Canada north of ~60°N). Further investigation of these places using an independent dataset and/or methodology should be planned.

Similarly, for the 90 km depth, the average V_s of our model is 0.14 and 0.17 km/s slower than that of NA04 and NA07 models, respectively (Figure 16). The standard deviation stays almost unchanged (0.17 for NA04 and 0.16 for NA07), and many of the nodes with V_s differences exceeding one standard deviation are the same ones as identified at the 70-km depth. This suggests that the difference between our tomography model and those derived from earthquake data is probably systematic and strongly data dependent.

5. Implications and Discussion

Shear velocity is one of the fundamental physical properties characteristic of earth materials. It is strongly linked to composition and state such as temperature and in turn to the patterns of present deformation and evolutionary history of tectonic/geological structures. 3D velocity tomography is especially useful in delineating deep structures and assessing their tectonic implications. Although a comprehensive discussion of the various tectonic implications of our ambient seismic noise tomography is both important and desirable, it is impractical to include everything in this article. We therefore limit the discussion to topics directly relevant to our data and seismological results. Other important subjects for which our data provide new constraints, such as the temperature variations in the lithosphere across different tectonic/geologic provinces and the density distribution within the crust and uppermost mantle, require additional analysis and will be covered in a subsequent article.

5.1. Surface Geology and Topography of the Crust–mantle Transition

In general, the surface geology of Canada (south of 70°N) can be divided into five components, namely, the Cascadia forearc, the North America Cordillera, the sedimentary basins overlying the craton (i.e., the Interior Platform and the Hudson Bay Platform), the exposed craton (i.e., the Canadian Shield), and the Appalachian orogen [e.g., *Wheeler et al.*, 1997]. Previous crustal models have indicated that the Cascadia forearc and Cordillera are associated with relatively thin (~35 km and less) crust, whereas the crustal thickness in the stable craton region is 40–45 km [*Bassin et al.*, 2000; *Mooney et al.*, 1998; *Perry et al.*, 2002]. The significant differences in the average elevation and Moho depth have been explained as the thermal isostasy buoyancy effect due to higher lithospheric temperatures in the Cordillera [e.g., *Currie and Hyndman*, 2006; *Hyndman and Currie*, 2011].

While the average crustal thickness inferred from our tomography results is in good agreement with previous models, we notice that the Moho relief within each geological region, as manifest by the depth contours of 50% and 85% V_s increase from crust to uppermost mantle, is not as uniform as previously mapped (Figures 10–14). For example, the Moho depth beneath the Cordillera shows local variations that fluctuate between 25 and 38 km (e.g., Profile 1–1', Figure 12). Locations with particularly shallow crust–mantle transition generally coincide with known volcanic areas where the crustal structure is dominated by the corresponding volcanic processes. Presumably the Moho topography is also related to the mechanical strength/rigidity profile of the lithosphere, and may be controlled by the pattern of mantle flow beneath [*Currie and Hyndman*, 2006]. Although it is beyond the scope of this study to determine the exact physics implied by the Moho topography, our results suggest that the nature of the dominant process must involve factors that vary locally (i.e., on scales of 100–1000 km).

Even within the cratonic region east of the Cordillera, regional variations in the crustal thickness are observed (Figures 12 and 13). While the general trend of the Moho depth is to increase gradually from north to south, there are clear local highs and lows along the E–W direction (Profiles A–A', B–B', and C–C' in Figure 12, and Figures 13a and 13b). It is important to point out that previous studies on the effective elastic thickness of the lithosphere also show significant variations for different parts of the craton [e.g., *Burov et al.*, 1998; *Flück et al.*, 2003; *Hyndman et al.*, 2009; *Mareschal et al.*, 2005; *Wu*, 1991]. Such variations have been attributed to the strong lateral variations in the thermal regime of the lithosphere [*Flück et al.*, 2003; *Hyndman et al.*, 2009; *Wang and Mareschal*, 1999], large-scale crustal heterogeneity [*Burov et al.*, 1998; *Guillou-Frottier et al.*, 1996], or both [*Mareschal et al.*, 2005; *Wu*, 1991]. Our results suggest that the lateral variation of crustal structures, including the thickness, may also play a role in controlling the effective elastic thickness of the lithosphere.

5.2. Sharpness of the Crust–mantle Transition

The sharpness of a velocity interface can be characterized by two parameters: its thickness and the amount of velocity change. Given the same amount of velocity change, a sharp interface means that it is very thin with a large velocity jump whereas a diffused one spans a finite depth range with a gradual velocity variation. Most previous studies using global crustal models, however, have not adequately addressed the sharpness of the crust–mantle transition. Our results provide systematic estimates of the thickness and corresponding V_s increase of the crust–mantle transition for most of the North American continent north of 40°N that, in turn, would constrain interpretations of the formation and subsequent tectonic evolution of the continental crust.

It is interesting to point out that there seems to be a slight anti-correlation between the crust–mantle transition thickness $dZ_{50\%\text{-}85\%}$ and the amount of velocity change $dV_{50\%\text{-}85\%}$ (Figures 13c and 13f). Overall, the Canadian Shield is associated with a relatively smaller $dZ_{50\%\text{-}85\%}$ and a larger $dV_{50\%\text{-}85\%}$. As the $dZ_{50\%\text{-}85\%}$ increases from the Canadian Shield outward, the corresponding $dV_{50\%\text{-}85\%}$ decreases accordingly but the relationship is obviously not linear. One clear exception is the American mid-west region between 90°W and 100°W where both the $dZ_{50\%\text{-}85\%}$ and $dV_{50\%\text{-}85\%}$ are large.

It has been suggested that the structural details associated with the crust–mantle transition may be too complex and varied to prevent a single, universally applicable interpretation of the continental Moho discontinuity [*Cook et al.*, 2010]. In fact, a comprehensive compilation of "geophysical" Moho distribution from Lithoprobe data has concluded that the continental Moho discontinuity is not a simple boundary and may not always coincide with the petrological Moho [e.g., *Cook et al.*, 2010; *Moores*, 1982], although a large portion of Canada remains unexplored by Lithoprobe-type transects. Our ambient noise tomography results confirm that the crust–mantle transition is characterized by a finite zone whose thickness and velocity contrast may vary from one geological/tectonic region to another.

Nonetheless, if we take the seismic velocity as a reasonable proxy for the density and composition of crustal materials [*Christensen and Mooney*, 1995], then the sharpness of the ambient-noise Moho can be viewed as a first-order indicator of how much the position, geometry, and physical properties of the crust–mantle transition have been altered over the geological history. Further studies with high resolution at local and regional scales are obviously needed to better understand the geological and tectonic significance of the variation in the sharpness of the ambient-noise Moho.

5.3. Tectonic Significance of the Large Mid-Crust Velocity Gradients

The discovery of a common mid-crust velocity discontinuity, often called the Conrad discontinuity, was based on seismic signals refracted from a velocity interface located at a depth of 15–20 km with V_p of ~6.5 km/s [*Richter*, 1958]. Although it was originally interpreted to be the boundary between a granitic upper crust and a basaltic lower crust, later research indicated that such a simple interpretation could not explain the observed complexity [e.g., *Fountain and Christensen*, 1989]. Not only is the mid-crust discontinuity far less frequently observed than the Moho, but the corresponding seismic velocities are often not those of typical granitic or basaltic compositions [*Christensen and Mooney*, 1995].

One recent explanation for a mid-crustal boundary was provided by *Mazzotti and Hyndman* [2002] based on the distribution of regional seismicity, heat flow measurements, geodetic data, and numerical modeling of the northern Cordillera region. They proposed that the lower crust is very weak due to consistently high temperatures beneath the Cordillera. According to that model, a mid-crustal detachment zone is formed above the weakest point and facilitates the northeastward movement of the quasi-rigid upper crust overthrusting the craton. We speculate that the large mid-crust velocity gradients observed beneath the Cordillera, as described in Section 3.4, are also related to such mid-crustal detachment zones. The mid-crust velocity contrast in this region probably represents a thermodynamically controlled interface that may have played an important role in the regional thickskinned tectonics.

For the large mid-crust velocity gradient beneath part of the Canadian Shield (Figures 10, 13, and 14), the most straightforward interpretation would be a rheological boundary between the upper and lower crust formed at earlier times when temperatures were much higher. The corresponding velocity difference may be explained by a change of composition from an average mix of 45% granitic gneiss and 5% amphibolite at the upper crust depths to 15% granitic gneiss and 35% amphibolite in the lower crust [*Christensen and Mooney*, 1995]. Depending on other possible factors such as the depth of the discontinuity and its sharpness, the exact compositional ratio may vary from one place to another.

5.4. Possible Effect of Anisotropy

The velocity structures derived from our tomography inversion are assumed isotropic. This assumption is obviously too simplistic for places where azimuthal anisotropy has been demonstrated previously, such as in Cascadia [*Currie et al.*, 2004; *Eakin et al.*, 2010; *Rieger and Park*, 2010], the Superior province [*Darbyshire et al.*, 2007], and the Appalachians [*Barruol et al.*, 1997; *Levin et al.*, 1999]. Based on earthquake data, *Yuan and Romanowicz* [2010] estimate the amount of azimuthal anisotropy in the upper mantle beneath the North America craton to be of the order of 1%.

In a recent global earthquake surface wave dispersion study, *Nettles and Dziewonski* [2008] pointed out that the transverse component of shear velocity (i.e., V_{SH}) is on average 2–6% faster than the radial component (V_{SV}) at the uppermost mantle depths beneath Canada. Using the dense US Transportable Array ambient noise data, *Moschetti et al.* [2010b] concluded that the mean amplitude of radial anisotropy in the lower crust and upper mantle beneath the western US are 3.6% and 5.3%, respectively. Because both NA04 and NA07 models are derived from inversion of shear and Rayleigh waveforms of moderate-magnitude (M_s≥~5) regional earthquakes located around the periphery of the North America continent, the reported V_s values presumably represent the isotropic V_s, which is approximately the mean of V_{SH} and V_{SV}. In contrast, the V_s values determined in our study are in fact

V_{SV} because our dataset contains only Rayleigh waves. Therefore, a 2–6% radial anisotropy at the uppermost mantle would yield a velocity reduction of 0.05–0.14 km/s between our results and the two previous models. This estimate appears to be somewhat smaller than that shown in Figure 16. Further studies to characterize the amount and distribution of both azimuthal and radial anisotropy beneath Canada are needed.

5.5. Future Efforts

Although the dataset used in constructing NA07 has considerably more ray paths due to additional earthquake sources and the deployment of the temporary US Transportable Array, the data coverage for Canada is still not ideal. Nonetheless, a big advantage of earthquake data is that the seismic energy can penetrate to great depths, and thus earthquake tomography is often capable of resolving deep structures. In contrast, ambient seismic noise tomography does not require well-distributed earthquake sources but the data generally do not have sufficient low-frequency energy to resolve velocity anomalies at depth.

One possible effort is to take a hybrid approach to integrate the data constraints from both earthquake and ambient noise sources. We have experimented with this approach by incorporating a small set of earthquake dispersion curves [*Darbyshire*, 2005; *Darbyshire et al.*, 2007] into our analysis, but with limited success. Taking the phase velocity measurements for the station pair of ATGO and ATKO for example, the dispersion curve derived from ambient seismic noise has good S/N in the 3–23 s period range, whereas the dispersion curve from earthquake data spans 24–186 s. However, there is a sudden 0.1 km/s jump between the upper end of the ambient-noise dispersion curve and the lower end of the earthquake one.

We suspect the jump as an artifact arising from the different processing procedures and controlling parameters employed in different studies (e.g., the assumed number of cycles between station pairs). Several recent efforts of joint interpretation of ambient seismic noise and earthquake dispersion data also observed a discrepancy between earthquake and ambient noise dispersion curves, although the disagreement was smaller and diminished as more earthquake measurements are added to the dataset [e.g., *Moschetti et al.*, 2010a; *Shen et al.*, 2013; *Zhou et al.*, 2012]. In other words, it might not be appropriate to simply combine dispersion measurements found in the literature with the seismic ambient noise dispersion curves to form a hybrid dataset. A systematic and uniform re-processing of an expanded dataset is probably necessary to ensure their internal consistency.

A logical next step to better resolve the crustal thickness and velocity structures of our model is to combine constraints from dispersion data and other types of measurements that are more sensitive to velocity contrast at depths. This can be achieved, for example, by jointly inverting receiver functions with dispersion curves, as demonstrated by the recent study of *Shen et al.* [2013] for the central and western US. A similar effort for Canada is planned in the near future.

Finally, our results can provide important constraints on the density distribution within the crust. Given the relatively flat surface topography throughout most of the cratonic region, the observed relief of the crust–mantle transition cannot be interpreted as an Airy isostatic effect. Furthermore, an overall correlation between a relatively thick crust (>40 km) and a relatively high Moho V_s (≥4.25 km/s) can be established for the cratonic region (Figure 13). Such correlation could be qualitatively explained in terms of local density variations according to the linear velocity–density relationship determined from laboratory data for continental crustal materials [*Christensen and Mooney*, 1995]. However, a quantitative approach to determine the density and temperature distributions from our tomography model is not straightforward: that analysis is the focus of a forthcoming paper [*Currie et al.*, 2013, manuscript in preparation].

6. Conclusions

The long geological evolution of Canada has involved many tectonic processes operating over an area of 10 million km^2 and a timespan of 4 Gyr. This paper presents the first continental-scale study of the shear-velocity structure of Canada and the adjacent region using ambient noise tomography, providing better resolution and more homogeneous coverage than previous tomographic studies based on earthquake waveforms.

The vertical component of continuous waveform data between 2003 and 2009 from 788 broadband seismograph stations in Canada and adjacent regions are collected and processed following the procedures described in *Bensen et al.* [2007]. Stacked cross correlation functions of all station pairs are analyzed with a phase-matching filter to obtain both the group and phase-velocity dispersion curves of the Rayleigh wave. The dispersion measurements for regions overlapping with previous studies are consistent with published results and our results indicate that improvement in the signal-to-noise ratio of the stacked waveforms becomes marginal once the amount of data exceeds 3 years.

Surface-wave tomography inversion is carried out from the dispersion data to estimate the phase and group velocity distribution at 1° interval for periods between 5 and 100 s. In general, the patterns of group and phase velocity distributions are similar to each other at all periods. At shorter periods (e.g., 10 s), prominent low-velocity anomalies are observed in the Gulf of St. Lawrence in the east, the sedimentary basins of west Canada and the Cordillera. In contrast, the Canadian Shield exhibits high velocities. The velocity contrast between high and low anomalies becomes smaller at longer periods (e.g., ≥35 s), and the high velocities associated with the craton appear to expand slightly toward the west under the western Canadian sedimentary basin.

For each grid point, a 1D shear-velocity (V_s) profile is inverted from the dispersion data using the Neighbourhood Algorithm [*Sambridge*, 1999a; *Sambridge*, 1999b]. The resulted 4949 V_s profiles are then combined into a pseudo-3D V_s model that extends down to ~100-km depth. Overall, the inner part of the Canadian Shield has V_s consistently lower than that of the outer rim throughout the mantle depths resolvable by our data.

To better characterize the nature of crust–mantle transition, we propose that both the thickness and the amount of velocity increase should be included in addition to the depth and velocity of the Moho discontinuity. In this study, the "ambient noise" Moho is defined as the depth where the V_s increase is 85% from the typical value in the lower crust to uppermost mantle ($Z_{85\%}$ and $V_{85\%}$ in Figure 13). Such defined Moho is slightly different from other types (e.g., reflection Moho, refraction Moho, or electric Moho), but the difference is generally less than 5 km. The thickness of crust–mantle transition is defined as the depth difference between places where the crust–mantle V_s increase is 50% and 85% (the $dZ_{50\%\text{-}85\%}$ in Figure 13). We have observed considerable variations in the depth, V_s, and sharpness of the crust–mantle transition across Canada. For the cratonic region, an overall correlation among the crustal thickness, Moho V_s, and the thickness of the transition can be recognized except in the Hudson Bay area where the Moho V_s is relatively low. Such correlation does not seem to hold for the Canadian Cordillera, either, where a modestly sharp transition is associated with thin crust and low Moho V_s.

Prominent mid-crust V_s gradient is observed beneath the Cordillera and in the craton beneath part of the Canadian Shield. While the mid-crust velocity contrast beneath the Cordillera may be related to a detachment zone due to the consistently high temperature beneath, the large mid-crust velocity gradient beneath the Canadian Shield could be interpreted as a rheological boundary between the upper and lower crust with an average mix of 45% granitic gneiss and 5% amphibolite in the upper crust and 15% granitic gneiss and 35% amphibolite in the lower crust.

Quantitative comparison of our tomography results with previous earthquake-based tomography models reveals that the V_s derived from ambient seismic noise is slightly lower (by ~0.2 km/s at the 70 and 90-km depths). This is likely caused by the effect of radial anisotropy in the uppermost. An attempt to build a hybrid dataset containing dispersion measurements from both ambient noise and earthquakes was not successful because the measurements are internally inconsistent. A systematic and uniform re-processing of an expanded dataset is probably necessary for this approach to work. Other research efforts in our plan include extending the current study to Love waves, characterizing the amount and distribution of both azimuthal and radial anisotropy beneath Canada, and estimating the density and temperature distributions from our tomography model.

Acknowledgment

Fiona Darbyshire kindly provides the dispersion measurements of earthquake surface waves. Digital waveform data are obtained from the data centers of the Canadian Hazard Information Service and Incorporated Research Institutions for Seismology. We benefit from discussion with David Schneider, Sonya Dehler, and Yu-Lien Yeh. YB and JT acknowledge the support of the Marsden Fund of the Royal Society of New Zealand. MHR acknowledges support from US NSF grant EAR-1252085. This research is partially supported by a NSERC grant to HK (RGPIN 418268-2013). ESS contribution number XXXXXX.

Electronic Supplement 1: An ASCII file listing our tomography inversion results.

Electronic Supplement 2: An ASCII file listing physical parameters of the ambient-noise Moho determined in this study.

References

Adams, L. H., and E. D. Williamson (1923), Density distribution of the Earth, *Journal of the Washington Academy of Sciences*, *13*, 413-428.

Audet, P., and J. C. Mareschal (2004), Variations in elastic thickness in the Canadian Shield, *Earth Planet. Sci. Lett.*, *226*, 17-31, doi: 10.1016/j.epsl.2004.1007.1035.

Bank, C.-G., M. G. Bostock, R. M. Ellis, and J. F. Cassidy (2000), A reconnaissance teleseismic study of the upper mantle and transition zone beneath the Archean Slave craton in NW Canada, *Tectonophysics*, *319*(3), 151-166, doi:110.1016/S0040-1951(1000)00034-00032.

Barmin, M. P., M. H. Ritzwoller, and A. L. Levshin (2001), A fast and reliable method for surface wave tomography, *Pure Appl. Geophys.*, *158*, 1351-1375.

Barruol, G., P. G. Silver, and A. Vauchez (1997), Seismic anisotropy in the eastern United States: Deep structure of a complex continental plate, *J. Geophys. Res.*, *102*, 8329–8348.

Bassin, C., G. Laske, and G. Masters (2000), The current limits of resolution for surface wave tomography in North America, *EOS Trans AGU*, *81*, F897.

Bedle, H., and S. van der Lee (2009), S velocity variations beneath North America, *J. Geophys. Res.*, *114*(B7), B07308, doi:07310.01029/02008JB005949.

Behr, Y., J. Townend, S. Bannister, and M. K. Savage (2010), Shear-velocity structure of the Northland Peninsula, New Zealand, inferred from ambient noise correlations, *J. Geophys. Res.*, doi: 10.1029/2009JB006737.

Behr, Y., J. Townend, S. Bannister, and M. K. Savage (2011), Crustal shear wave tomography of the Taupo Volcanic Zone, New Zealand, via ambient noise correlation between multiple three-component networks, *Geochem. Geophy. Geosy.*, *12*, Q03015, doi:03010.01029/02010GC003385.

Bensen, G. D., M. H. Ritzwoller, and N. M. Shapiro (2008), Broadband ambient noise surface wave tomography across the United States, *J. Geophys. Res.*, *113*, B05306, doi:05310.01029/02007JB005248.

Bensen, G. D., M. H. Ritzwoller, and Y. Yang (2009), A 3-D shear velocity model of the crust and uppermost mantle beneath the United States from ambient seismic noise, *Geophys. J. Int.*, *177*(3), 1177-1196.

Bensen, G. D., M. H. Ritzwoller, M. P. Barmin, A. L. Levshin, F. Lin, M. P. Moschetti, N. M. Shapiro, and Y. Yang (2007), Processing seismic ambient noise data to obtain reliable broad-band surface wave dispersion measurements, *Geophys. J. Int.*, *169*, 1239-1260, doi: 1210.1111/j.1365-1246X.2007.03374.x.

Brown, D., S. Llana-Funez, R. Carbonell, J. Alvarez-Marron, D. Marti, and M. Salisbury (2009), Laboratory measurements of P-wave and S-wave velocities across a surface analog of the continental crust–mantle boundary: Cabo Ortegal, Spain, *Earth Planet. Sci. Lett.*, *285*(1–2), 27-38.

Burov, E., C. Jaupart, and J. C. Mareschal (1998), Large-scale crustal heterogeneities and lithospheric strength in cratons, *Earth Planet. Sci. Lett.*, *164*(1-2), 205-219.

Cannon, W. F., et al. (1989), The North American Midcontinent Rift beneath Lake Superior from GLIMPCE seismic reflection profiling, *Tectonics*, *8*(2), 305-332.

Cassidy, J. F. (1995), Review: Receiver function studies in the southern Canadian Cordillera, *Can. J. Earth Sci.*, *32*, 1514-1519.

Catchings, R. D., and W. D. Mooney (1991), Basin and Range crustal and upper mantle structure, northwest to central Nevada, *J. Geophys. Res.*, *96*(B4), 6247-6267.

Cheng, L. Z., J. C. Mareschal, C. Jaupart, F. Rolandone, C. Gariépya, and M. Radigon (2002), Simultaneous inversion of gravity and heat flow data: constraints on thermal regime, rheology and evolution of the Canadian Shield crust, *J. Geodyn.*, *34*, 11-30, doi:10.1016/S0264-3707(1001)00082-00085.

Christensen, N. I. (1996), Poisson's ratio and crustal seismology, *J. Geophys. Res.*, *101*, 3139-3156.

Christensen, N. I., and W. D. Mooney (1995), Seismic velocity structure and composition of the continental crust: A global view, *J. Geophys. Res.*, *100*, 9761-9788.

Clowes, R. M., P. T. C. Hammer, G. Fernandez-Viejo, and J. K. Welford (2005), Lithospheric structure in northwestern Canada from Lithoprobe seismic refraction and related studies; a synthesis, *Can. J. Earth Sci.*, *42*(6), 1277-1293.

Clowes, R. M., A. G. Green, C. J. Yorath, E. R. Kanasewich, G. F. West, and G. D. Garland (1984), LITHOPROBE - a national program for studying the third dimension of geology, *J. Can. Soc. Exp. Geophys.*, *20*, 23-39.

Cook, F. (2002), Fine structure of the continental reflection Moho, *Geol. Soc. Am. Bull.*, *114*(1), 64-79.

Cook, F. A., D. J. White, A. G. Jones, D. W. S. Eaton, J. Hall, and R. M. Clowes (2010), How the crust meets the mantle; Lithoprobe perspectives on the Mohorovicic discontinuity and crust-mantle transition, *Can. J. Earth Sci.*, *47*(4), 315-351, doi:310.1139/E1109-1076.

Currie, C. A., and R. D. Hyndman (2006), The thermal structure of subduction zone back arcs, *J. Geophys. Res.*, *111*, B08404, doi:08410.01029/02005JB004024.

Currie, C. A., J. F. Cassidy, R. D. Hyndman, and M. G. Bostock (2004), Shear wave anisotropy beneath the Cascadia subduction zone and western North American craton, *Geophys. J. Int.*, *157*, 341-353, doi: 310.1111/j.1365-1246X.2004.02175.x.

Dalton, C. A., G. Ekström, and A. M. Dziewonski (2009), Global seismological shear velocity and attenuation: A comparison with experimental observations, *Earth Planet. Sci. Lett.*, *284*, 65-75, doi:10.1016/j.epsl.2009.1004.1009.

Darbyshire, F. A. (2005), Upper mantle structure of Arctic Canada from Rayleigh wave dispersion, *Tectonophysics*, *405*, 1-23.

Darbyshire, F. A., D. W. Eaton, A. W. Frederiksen, and L. Ertolahti (2007), New insights into the lithosphere beneath the Superior Province from Rayleigh wave dispersion and receiver function analysis, *Geophys. J. Int.*, *169*, 1043-1068, doi: 1010.1111/j.1365-1246X.2006.03259.x.

Dunkin, J. W. (1965), Computation of modal solutions in layered, elastic media at high frequencies, *Bull. Seismol. Soc. Am.*, *55*, 335-358.

Dziewonski, A. M., and D. L. Anderson (1981), Preliminary reference Earth model, *Phys. Earth Planet. Inter.*, *25*, 297-356.

Eakin, C. M., M. Obrebski, R. M. Allen, D. C. Boyarko, M. R. Brudzinski, and R. Porritt (2010), Seismic anisotropy beneath Cascadia and the Mendocino triple junction; interaction of the subducting slab with mantle flow, *Earth Planet. Sci. Lett.*, *297*(3-4), 627-632.

Flück, P., R. D. Hyndman, and C. Lowe (2003), Effective elastic thickness Te of the lithosphere in western Canada, *J. Geophys. Res.*, *108*(B9), 2430, doi:2410.1029/2002JB002201.

Fountain, D. M., and N. Christensen (Eds.) (1989), *Composition of the continental crust and upper mantle: a review*, 711-742 pp., GSA Mem.

Frederiksen, A. W., M. G. Bostock, J. C. VanDecar, and J. F. Cassidy (1998), Seismic structure of the upper mantle beneath the northern Canadian Cordillera from teleseismic travel-time inversion, *Tectonophysics*, *294*, 43-55.

Frederiksen, A. W., S.-K. Miong, F. A. Darbyshire, D. W. Eaton, S. Rondenay, and S. Sol (2007), Lithospheric variations across the Superior Province, Ontario, Canada: Evidence from tomography and shear wave splitting, *J. Geophys. Res.*, *112*, B07318, doi:07310.01029/02006JB004861.

Fulton, R. J. (1989), *Quaternary Geology of Canada and Greenland: Maps*, International Specialized Book Service Incorporated.

Green, D. H., and A. E. Ringwood (1972), A comparison of recent experimental data on the gabbro-garnet granulite-eclogite phase transition, *J. Geology*, *80*(3), 277-288. doi:210.1086/627731.

Guillou-Frottier, L., C. Jaupart, J. C. Mareschal, C. Gariépy, G. Bienfait, L. Z. Cheng, and R. Lapointe (1996), High heat flow in the trans-Hudson Orogen, Central Canadian Shield, *Geophys. Res. Lett.*, *23*(21), 3027-3030, doi:3010.1029/3096GL02895.

Hyndman, R. D., and T. S. Lewis (1999), Geophysical consequences of the Cordillera-Craton thermal transition in southwestern Canada, *Tectonophysics*, *306*, 397-422, doi:310.1016/S0040-1951(1099)00068-00062.

Hyndman, R. D., and C. A. Currie (2011), Why is the North America Cordillera high? Hot backarcs, thermal isostasy, and mountain belts, *Geology*, *39*(8), 783-786, doi:710.1130/G31998.31991.

Hyndman, R. D., C. A. Currie, S. Mazzotti, and A. Frederiksen (2009), Temperature control of continental lithosphere elastic thickness, Te vs Vs, *Earth Planet. Sci. Lett.*, *277*, 539-548.

Hyndman, R. D., P. Flück, S. Mazzotti, T. J. Lewis, J. Ristau, and L. Leonard (2005), Current tectonics of the northern Canadian Cordillera, *Can. J. Earth Sci.*, *42*, 1117-1136, doi:1110.1139/E1105-1023.

Ito, K., and G. C. Kennedy (1971), An experimental study of the basalt–garnet granulite–eclogite transition, in *The Earth beneath the continents*, edited by J. G. Heacock, pp. 303-314, AGU Geophysical Monograph 14, Washington, D. C.

Jones, A. G., and I. J. Ferguson (2001), The electric Moho, *Nature*, *409*(6818), 331-333.

Klemperer, S. L., T. A. Hauge, E. C. Hauser, J. E. Oliver, and C. J. Potter (1986), The Moho in the northern Basin and Range province, Nevada, along the COCORP 400N seismic reflection transect, *Geol. Soc. Am. Bull.*, *97*(5), 603-618.

Lebedev, S., and R. D. van der Hilst (2008), Global upper-mantle tomography with the automated multimode inversion of surface and S-wave forms, *Geophys. J. Int.*, *173*, 505-518, doi: 510.1111/j.1365-1246X.2008.03721.x.

Lebedev, S., J. M. C. Adam, and T. Meier (2013), Mapping the Moho with seismic surface waves: A review, resolution analysis, and recommended inversion strategies, *Tectonophysics*, *in press*.

Lekic, V., and B. Romanowicz (2011), Tectonic regionalization without a priori information; a cluster analysis of upper mantle tomography, *Earth Planet. Sci. Lett.*, *308*(1-2), 151-160.

Leveque, J.-J., L. Rivera, and G. Wittlinger (1993), On the use of the checker-board test to assess the resolution of tomographic inversion, *Geophys. J. Int.*, *115*, 313-318.

Levin, V., W. Menke, and J. Park (1999), Shear wave splitting in the Appalachians and the Urals: A case for multilayered anisotropy, *J. Geophys. Res.*, *104*, 17,975-917,993.

Levshin, A. L., and M. H. Ritzwoller (2001), Automated detection, extraction, and measurement of regional surface waves, *Pure Appl. Geophys.*, *158*(8), 1531-1545.

Lin, F.-C., M. P. Moschetti, and M. H. Ritzwoller (2008), Surface wave tomography of the Western United States from ambient seismic noise; Rayleigh and Love wave phase velocity maps, *Geophys.*

J. Int., *173*(1), 281-298, doi:210.1111/j.1365-1246X.2008.03720.x.

Lin, F.-C., M. H. Ritzwoller, J. Townend, S. Bannister, and M. Savage (2007), Ambient noise Rayleigh wave tomography of New Zealand, *Geophys. J. Int.*, dio:10.1111/j.1365-1246X.2007.03414x.

Ma, K.-F., Y.-Y. Lin, S.-J. Lee, J. Mori, and E. E. Brodsky (2012), Isotropic events observed with a borehole array in the Chelungpu fault zone, Taiwan, *Science*, *337*(459), 459-463, doi:410.1126/science.1222119.

Mareschal, J. C., C. Jaupart, F. Rolandone, C. Gariépy, C. M. R. Fowler, G. Bienfait, C. Carbonne, and R. Lapointe (2005), Heat flow, thermal regime, and elastic thickness of the lithosphere in the Trans-Hudson Orogen, *Can. J. Earth Sci.*, *42*(4), 517-532, doi:510.1139/e1104-1088.

Mazzotti, S., and R. D. Hyndman (2002), Yakutat collision and strain transfer across the northern Canadian Cordillera, *Geology*, *30*, 495-498.

Mercier, J.-P., M. G. Bostock, J. F. Cassidy, K. Dueker, J. B. Gaherty, E. J. Garnero, J. Revenaugh, and G. Zandt (2009), Body-wave tomography of western Canada, *Tectonophysics*, *475*, 480-492, doi:410.1016/j.tecto.2009.1005.1030.

Mohorovicic, A. (1910), Das Beben Vom 8. x. 1909, *Jahrbuch Meterologie Observatorie Zagrab*, *Vol. 9*, 1-63.

Mooney, W. D. (1987), Seismology of the continental crust and upper mantle, *Rev. Geophys.*, *25*, 1168-1176.

Mooney, W. D., and T. M. Brocher (1987), Coincident seismic reflection/refraction studies of the continental lithosphere: a global review, *Rev. Geophys.*, *25*, 723-742.

Mooney, W. D., G. Laske, and T. G. Masters (1998), CRUST 5.1: A global crustal model at 5° x 5°, *J. Geophys. Res.*, *103*, 727-747.

Moores, E. M. (1982), Origin and emplacement of ophiolites, *Rev. Geophys. Space Phys.*, *20*(4), 735-760.

Moschetti, M. P., M. H. Ritzwoller, F. C. Lin, and Y. Yang (2010a), Crustal shear wave velocity structure of the Western United States inferred from ambient seismic noise and earthquake data, *J. Geophys. Res.*, *115*(B10), B10306, doi:10310.11029/12010JB007448.

Moschetti, M. P., M. H. Ritzwoller, F. Lin, and Y. Yang (2010b), Seismic evidence for widespread Western-US deep-crustal deformation caused by extension, *Nature*, *464*(7290), 885-889.

Nettles, M., and A. M. Dziewonski (2008), Radially anisotropic shear velocity structure of the upper mantle globally and beneath North America, *J. Geophys. Res.*, *113*, B02303, doi:02310.01029/02006JB004819.

Okulitch, A. V., and H. Trettin (1991), Late Cretaceous to Early Tertiary deformation, Arctic Islands, in *Geology of the Innuitian Orogen and Arctic Platform of Canada and Greenland*, edited by H. P. Trettin, pp. 469-489, Geol. Surv. Canada, Ottawa.

Pawlak, A., D. W. Eaton, I. D. Bastow, J.-M. Kendall, G. Helffrich, J. Wookey, and D. Snyder (2010), Crustal structure beneath Hudson Bay from ambient-noise tomography: implications for basin formation, *Geophys. J. Int.*, *181*, 65-82, doi: 10.1111/j.1365-1246X.2010.04828.x.

Perry, H. K. C., D. W. S. Eaton, and A. M. Forte (2002), LITH5.0: a revised crustal model for Canada based on Lithoprobe results, *Geophys. J. Int.*, *150*, 285-294.

Perry, H. K. C., C. Jaupart, J.-C. Mareschal, and G. Bienfait (2006), Crustal heat production in the Superior Province, Canadian Shield, and in North America inferred from heat flow data, *J. Geophys. Res.*, *111*, B04401, doi:04410.01029/02005JB003893.

Richter, C. F. (1958), *Elementary Seismology*, 712 pp., Freeman, San Francisco, Calif.

Rieger, D. M., and J. Park (2010), USArray observations of quasi-Love surface wave scattering; orienting anisotropy in the Cascadia plate boundary, *J. Geophys. Res.*, *115*(B5), B05306, doi:05310.01029/02009jb006754.

Ritzwoller, M. H., F.-C. Lin, and W. Shen (2011), Ambient noise tomography with a large seismic array, *Comptes Rendus Geoscience*, *343*, 558-570, doi:510.1016/j.crte.2011.1003.1007.

Sabra, K. G., P. Gerstoft, P. Roux, W. A. Kuperman, and M. C. Fehler (2005), Surface wave tomography from microseisms in Southern California, *Geophys. Res. Lett.*, *32*(14), L14311, doi:14310.11029/12005GL023155.

Sambridge, M. (1999a), Geophysical Inversion with a Neighbourhood Algorithm -II. Appraising the ensemble, *Geophys. J. Int.*, *138*, 727-746.

Sambridge, M. (1999b), Geophysical inversion with a neighbourhood algorithm - I. Searching a parameter space, *Geophys. J. Int.*, *138*, 479-494.

Shapiro, N. M., M. H. Ritzwoller, P. Molnar, and V. Levin (2004a), Thinning and flow of Tibetan crust constrained by seismic anisotropy, *Science*, *305*, 233-236. doi:210.1126/science.1098276.

Shapiro, N. M., M. H. Ritzwoller, J. C. Mareschal, and C. Jaupart (2004b), Lithospheric structure of the Canadian Shield inferred from inversion of surface-wave dispersion with thermodynamic a priori constraints, *Geol. Soc. London Special Pub.*, *239*, 175-194, doi:110.1144/GSL.SP.2004.1239.1101.1112.

Shapiro, N. M., M. Campillo, L. Stehly, and M. H. Ritzwoller (2005), High-resolution surface-wave tomography from ambient seismic noise, *Science*, *307*(5715), 1615-1618.

Shen, W., M. H. Ritzwoller, and V. Schulte-Pelkum (2013), A 3-D model of the crust and uppermost mantle beneath the Central and Western US by joint inversion of receiver functions and surface wave dispersion, *J. Geophys. Res. Solid Earth*, *118*, 1-15, doi:10.1029/2012JB009602.

Simmons, N. A., A. M. Forte, L. Boschi, and S. P. Grand (2010), GyPSuM; a joint tomographic model of mantle density and seismic wave speeds, *J. Geophys. Res.*, *115*(B12), B12310, doi:12310.11029/12010JB007631.

Simons, F., R. D. van der Hilst, J.-P. Montagner, and A. Zielhuis (2002), Multimode Rayleigh wave inversion for heterogeneity and azimuthal anisotropy of the Australian upper mantle, *Geophys. J.*

Int., *151*, 738-754.

Stehly, L., M. Campillo, and N. M. Shapiro (2006), A study of the seismic noise from its long-range correlation properties, *J. Geophys. Res.*, *111*(B10), B10306, doi:10310.11029/12005JB004237.

Steinhart, J. S. (1967), Mohorovicic discontinuity, in *International dictionary of geophysics*, edited by S. K. Runcorn, pp. 991–994, Pergamon Press, Oxford, UK.

Tibuleac, I. M., D. H. von Seggern, J. G. Anderson, and J. N. Louie (2011), Computing Green's functions from ambient noise recorded by accelerometers and analog, broadband, and narrow-band seismometers, *Seismol. Res. Lett.*, *82*(5), 661-675, doi:610.1785/gssrl.1782.1785.1661.

van der Lee, S., and A. Frederiksen (2005), Surface wave tomography applied to the North American upper mantle, in *Seismic Earth: Array Analysis of Broadband Seismograms*, edited by G. Nolet, pp. 67-80, AGU Geophysical Monograph 157, Washington, DC.

Vincent, J. (1989), Quaternary geology of the southeastern Canadian Shield, *Quaternary geology of Canada and Greenland*, *1*, 249-275.

Wang, Y., and J. Mareschal (1999), Elastic thickness of the lithosphere in the Central Canadian Shield, *Geophys. Res. Lett.*, *26*(19), 3033-3036, doi:3010.1029/1999GL010806.

Wapenaar, K., D. Draganov, and J. O. A. Robertsson (2008), *Seismic Interferometry: History and Present Status*, 628 pp., Soc. of Explor. Geophys., Tulsa, OK.

Wathelet, M. (2005), Array recordings of ambient vibrations: surface wave inversion, Ph.D. thesis, Faculté des Sciences Appliquées.

Wathelet, M. (2008), An improved neighborhood algorithm: Parameter conditions and dynamic scaling, *Geophys. Res. Lett.*, *35*, doi:10.1029/2008GL033256.

Wheeler, J. O., P. F. Hoffman, K. D. Card, A. Davidson, B. V. Sanford, A. V. Okulitch, and W. R. Roest (1997), Geological Map of Canada, *Map D1860A*.

Williams, H. (1979), Appalachian Orogen in Canada, *Can. J. Earth Sci.*, *16*(3), 792-807.

Wu, P. (1991), Flexure of lithosphere beneath the Alberta foreland basin: evidence of an eastward stiffening continental lithosphere, *Geophys. Res. Lett.*, *18*(3), 451-454.

Yuan, H., and B. Romanowicz (2010), Lithospheric layering in the North American Craton, *Nature*, *466*(7310), 1063-1068, doi:1010.1038/nature09332.

Zhou, L., J. Xie, W. Shen, Y. Zheng, Y. Yang, H. Shi, and M. H. Ritzwoller (2012), The structure of the crust and uppermost mantle beneath south China from ambient noise and earthquake tomography, *Geophys. J. Int.*, *189*(3), 1565-1583, doi: 1510.1111/j.1365-1246X.2012.05423.x.

Figure Caption

Figure 1. Topography map of Canada showing major geological and tectonic settings. Thick purple lines mark the boundaries between the Canadian Shield, where the Archean craton is exposed, and stable platforms, where sedimentary rocks are underlain by the craton. Thick red lines mark the boundaries between stable platforms and orogenic belts. Jdf: Juan de Fuca plate; ExP: Explorer plate; QCF: Queen Charlotte fault.

Figure 2. Station distribution and ray path coverage of our dataset. The color of the ray path varies with the inter-station distance (black indicates the longest paths, white the shortest) to better depict the path density of different regions. Red triangles mark the location of stations discussed in the text and subsequent figures.

Figure 3. Representative examples of stacked cross-correlation functions from continuous ambient seismic noise data. Locations of stations are shown in Figure 2.

Figure 4. Representative examples of stacked cross-correlation functions using various amount of ambient seismic noise (1 year: top trace; 3 years: middle trace; and 7 years: bottom trace). Notice that the improvement in signal-to-noise ratio becomes marginal once the amount of data exceeds 3 years. The result of frequency-time analysis (FTAN) is shown at the lower panel with the determined dispersion curve shown in white.

Figure 5. A comparison of the stacked cross-correlation functions (top trace), the symmetric component of the cross-correlation function (middle trace), and the dispersion measurement (bottom panel) for the station pair RLMT and NLWA. Our results (a) and those obtained from the IRIS Data Management Center (b) are nearly identical.

Figure 6. Surface wave tomography inversion results using ambient seismic noise data for the periods of 10 s (a), 35 s (b), and 50 s (c). For each period, the phase and group velocity distribution are shown at the top panels. The bottom panel shows the corresponding resolution length as determined from the spike-perturbation test (left) and the depth sensitivity kernel (calculated at the location of 55°N, 110°W).

Figure 7. Examples of 1D shear-velocity inversion for 4 representative grid points. The phase and group velocity dispersion curves are shown at the top and middle panels, respectively. The observed measurements are marked by black plus symbols, whereas the synthetics corresponding to the best-fitting model is shown in pink. The Neighbourhood Algorithm inversion results are shown at the bottom panel. The color of the model space represents the density distribution of samples. The solid and dashed black lines in the middle correspond to the weighted average and the best-fitting models, respectively. Red dashed lines mark the sampled model space.

Figure 8. Distribution of the root-mean-square (RMS) misfit of our Neighbourhood Algorithm inversion for the shear-velocity structure of Canada and adjacent regions.

Figure 9. Pseudo-3D tomography of Canada and its adjacent regions. The distribution of shear velocity at the depths of 5 km (a), 25 km (b), and 50 km (c) is displayed in color with red and blue corresponding to low and high values, respectively. White dashed lines on the 50-km image mark the location of cross sections shown in Figure 10, whereas small red circles and crosses correspond to the locations of velocity profiles shown in Figures 6 and 12, respectively.

Figure 10. Three east–west (A–A', B–B', and C–C') and three north–south (1–1', 2–2', 3–3') cross

sections showing pseudo-3D tomography of Canada. Color scale is the same as that in Figure 9. Vertical gradient of the V_s distribution is normalized and displayed as gray-scale shading overlaying the velocity images. The black and red lines correspond to the 50% and 85% V_s increase from crust to upper mantle, respectively, and effectively define the depth range of the crust–mantle transition. Geographic locations of the cross sections are marked in Figure 9c.

Figure 11. A schematic illustration on how the crust–mantle transition is characterized in this study. The lower crust shear velocity and the uppermost mantle shear velocities define the 0% and 100% of the V_s increase across the transition. Locations where the Vs increase reaches 50% and 85% are marked by blue and black crosses, respectively. Depth and shear velocity at the blue cross is inferred to be $Z_{50\%}$ and $V_{50\%}$. Depth and shear velocity at the black cross is inferred to be $Z_{85\%}$ and $V_{85\%}$.

Figure 12. Cross sections showing the distribution of crust–mantle transition delineated from ambient noise tomography results (gray zone). Locations of the Moho discontinuity reported in the CRUST2.0 and LITH5.0 models are plotted in dashed red and blue lines, respectively, for comparison.

Figure 13. Physical properties of the crust–mantle transition beneath Canada and the adjacent regions. (a) Depth contours corresponding to 50% shear-velocity increase from crust to upper mantle. (b) Depth contours corresponding to 85% shear-velocity increase from crust to upper mantle. (c) Thickness of the crust–mantle transition, which is the depth difference between (a) and (b). (d) Shear velocity at which the amount of increase is 50% from crust to upper mantle. (e) Similar to (d) but the amount of increase is 85%. (f) Amount of shear-velocity contrast across the crust–mantle transition, defined as the difference between (d) and (e).

Figure 14. Comparison of Lithoprobe seismic reflection profiles and the shear-velocity profiles of our tomography inversion at 10 selected grid nodes. The original Lithoprobe transect identifier is shown at the top of each reflection profile with the geographic coordinates of each grid node. The thick red and blue lines correspond to the weighted average and best-fitting models, respectively. Red circles mark

the location of "ambient noise" Moho which is defined as the location where shear-velocity increases by 85% from lower crust to upper mantle. Dashed orange lines mark the Moho depths in the LITH5.0 model that are primarily derived from Lithoprobe data. Thin blue lines mark the model uncertainty as determined from forward modeling.

Figure 15. Histograms showing the depth difference between the crustal model determined in this study and two previous models, CRUST2.0 (left) and LITH5.0 (right). $Z_{50\%}$, $Z_{75\%}$, $Z_{85\%}$, and $Z_{100\%}$ correspond to the depths where the increase of shear velocity is 50%, 75%, 85%, and 100% from the lower crust to the uppermost mantle. The mean value (avg) of all samples is given near the top-right corner of each plot. We use the $Z_{85\%}$ as a proxy for the "ambient noise Moho" because it yields the least overall difference with respect to both CRUST2.0 and LITH5.0 models.

Figure 16. Histograms showing the velocity difference between the velocity model determined in this study and two previous tomography models based on earthquake data, NA04 (left) and NA07 (right). The top and bottom correspond to the depth of 70 and 90 km, respectively. Overall, our results are slightly slower than those reported in previous models, as indicated by the mean value (avg) given near the top-right corner of each plot. This systematic difference is likely due to the effect of radial anisotropy in the upper mantle. See text for more details.

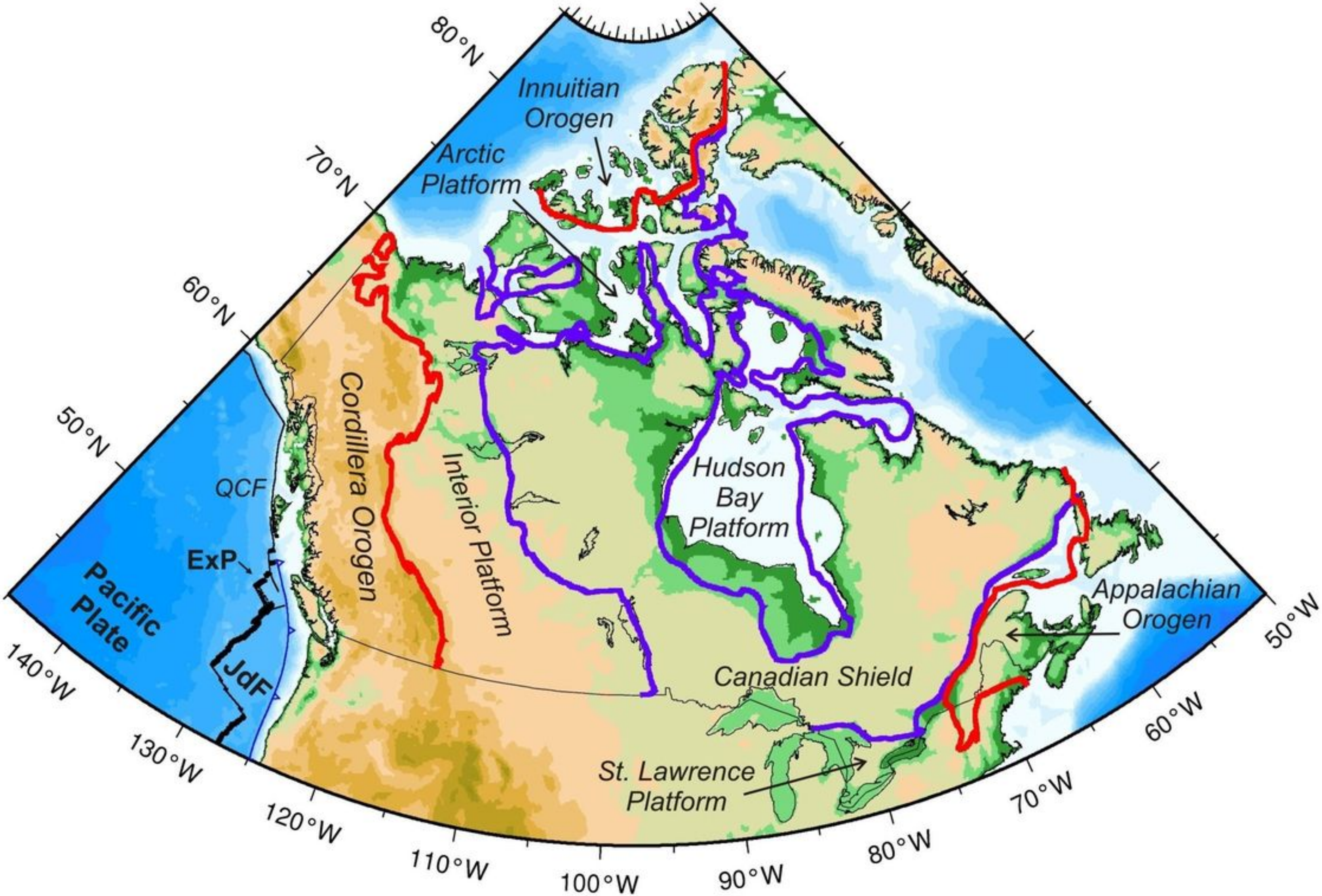

80°N
70°N
60°N
50°N
Innuitian Orogen
Arctic Platform
Cordillera Orogen
Interior Platform
Hudson Bay Platform
Canadian Shield
Appalachian Orogen
St. Lawrence Platform
QCF
ExP
JdF
Pacific Plate
140°W
130°W
120°W
110°W
100°W
90°W
80°W
70°W
60°W
50°W

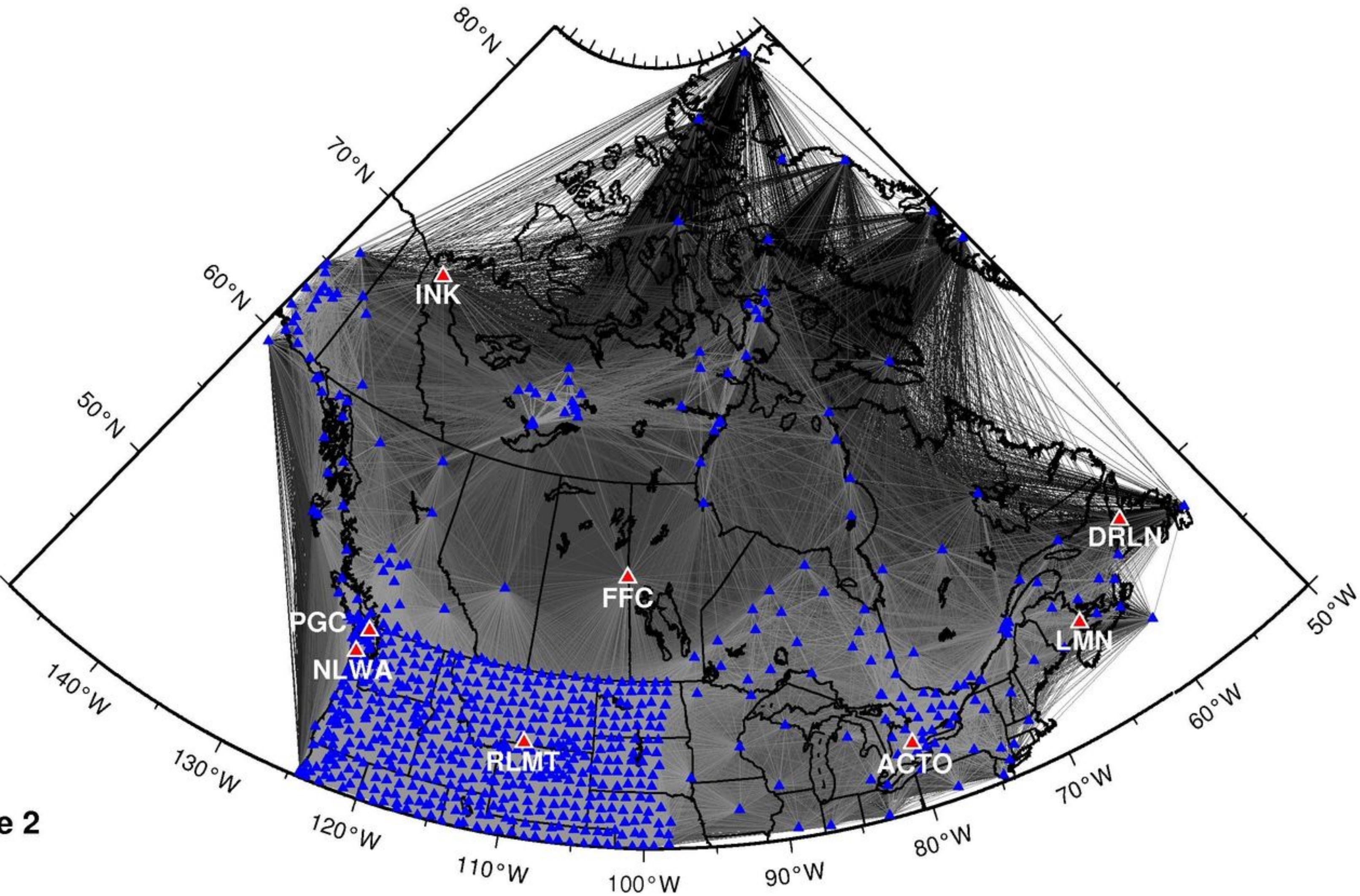
80°N
70°N
60°N
50°N
40°N
140°W
130°W
120°W
110°W
100°W
90°W
80°W
70°W
60°W
50°W
INK
DRLN
FFC
PGC
NLWA
LMN
RLMT
ACTO

Figure 2

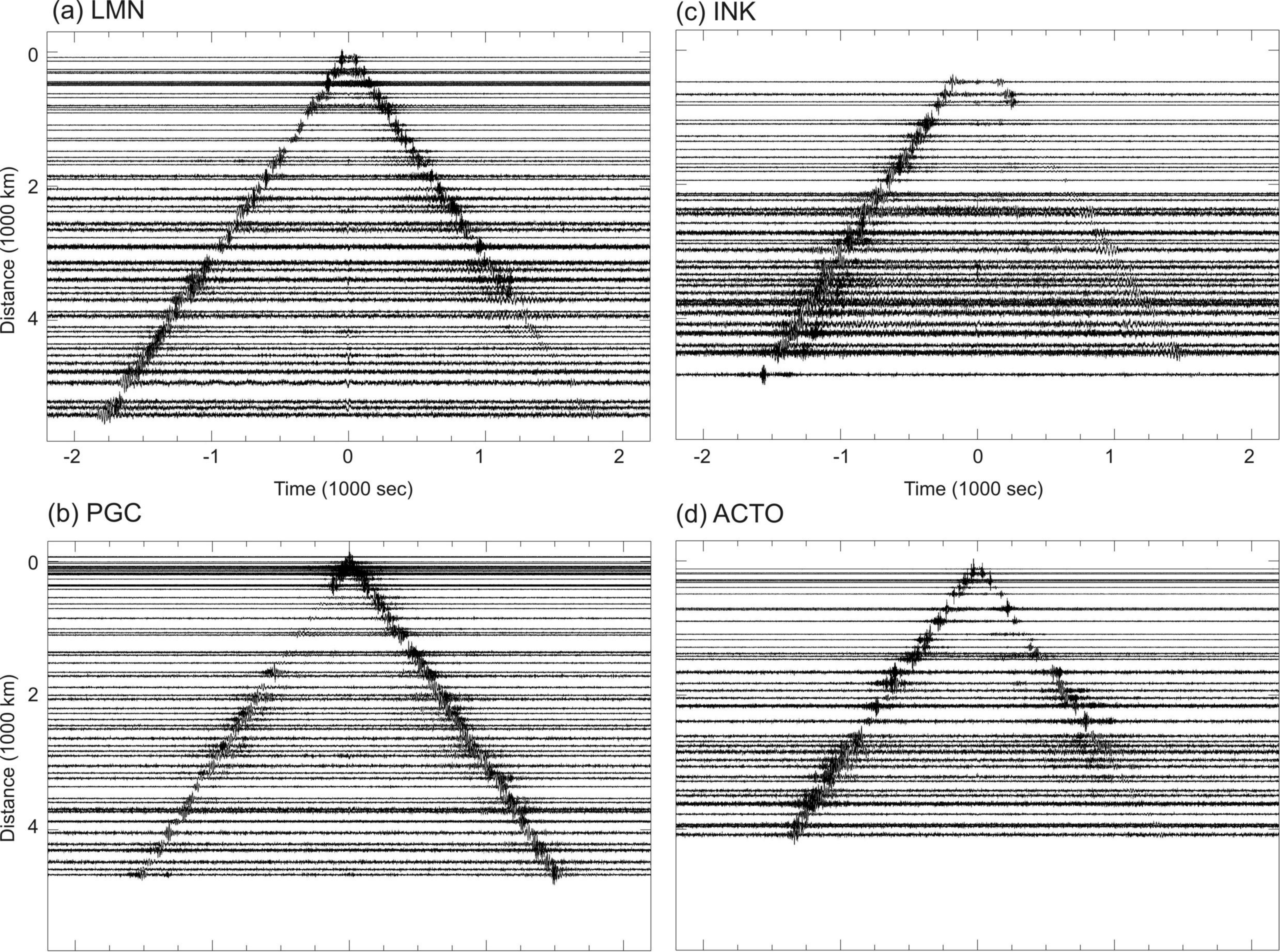
(a) LMN
(b) PGC
(c) INK
(d) ACTO
Distance (1000 km)
Time (1000 sec)
0
2
4
-2
-1
0
1
2

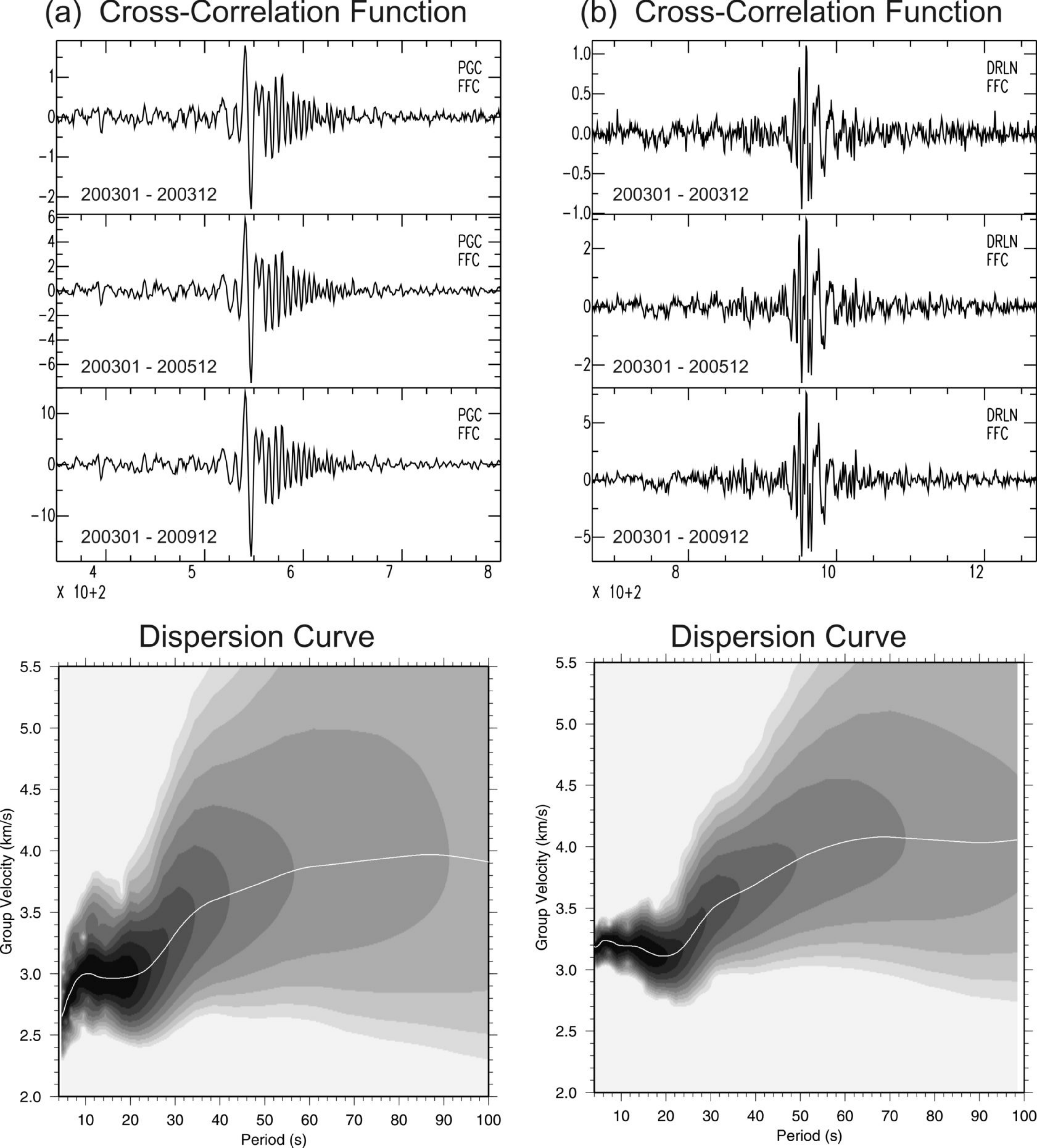

(a) Cross-Correlation Function
(b) Cross-Correlation Function
PGC
FFC
DRLN
FFC
200301 - 200312
200301 - 200512
200301 - 200912
X 10+2
Dispersion Curve
Group Velocity (km/s)
Period (s)

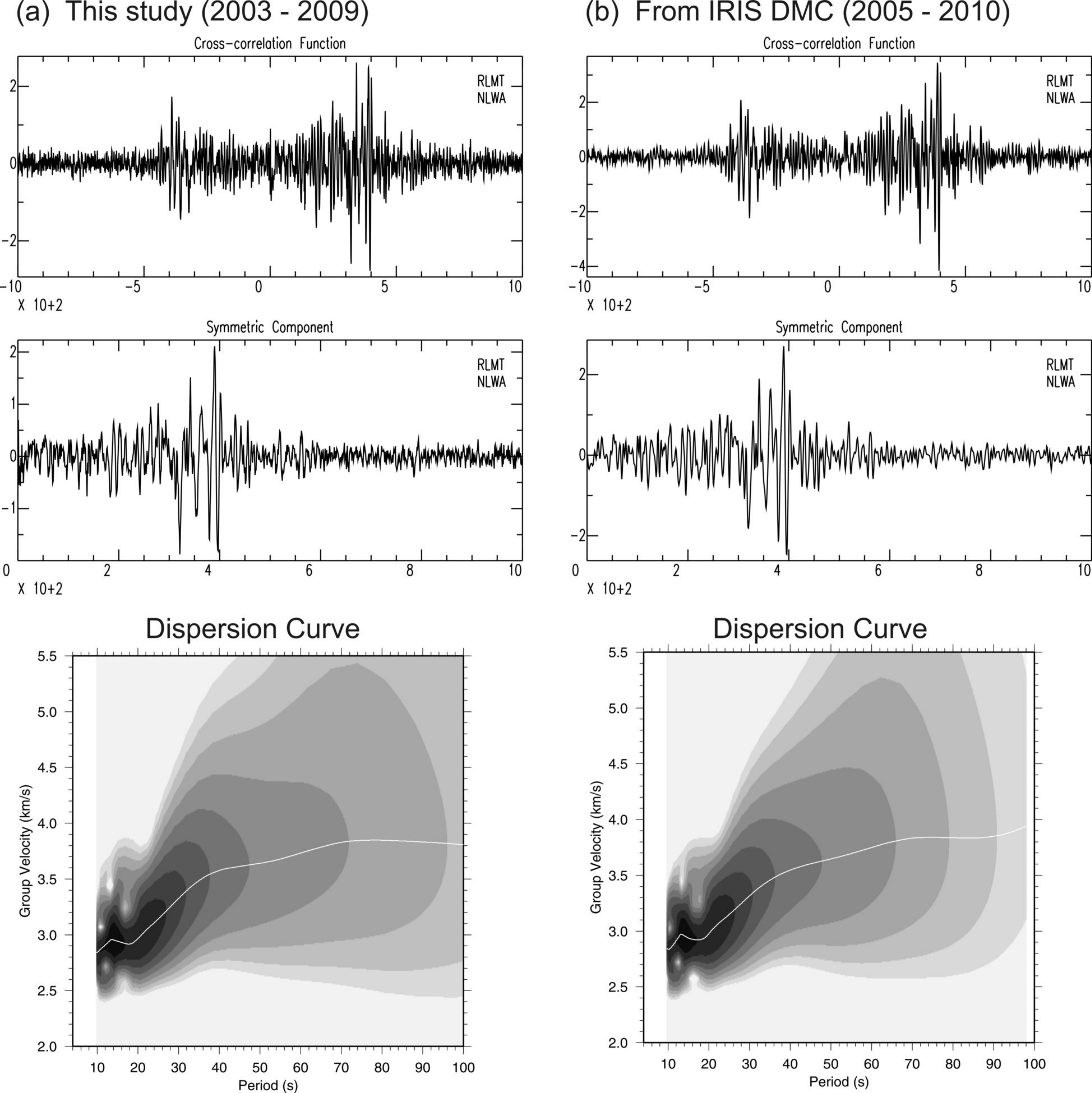

(a) This study (2003 - 2009)
Cross-correlation Function
RLMT
NLWA
X 10+2
Symmetric Component
RLMT
NLWA
X 10+2
Dispersion Curve
Group Velocity (km/s)
Period (s)
(b) From IRIS DMC (2005 - 2010)
Cross-correlation Function
RLMT
NLWA
X 10+2
Symmetric Component
RLMT
NLWA
X 10+2
Dispersion Curve
Group Velocity (km/s)
Period (s)

(a) Period = 10 s

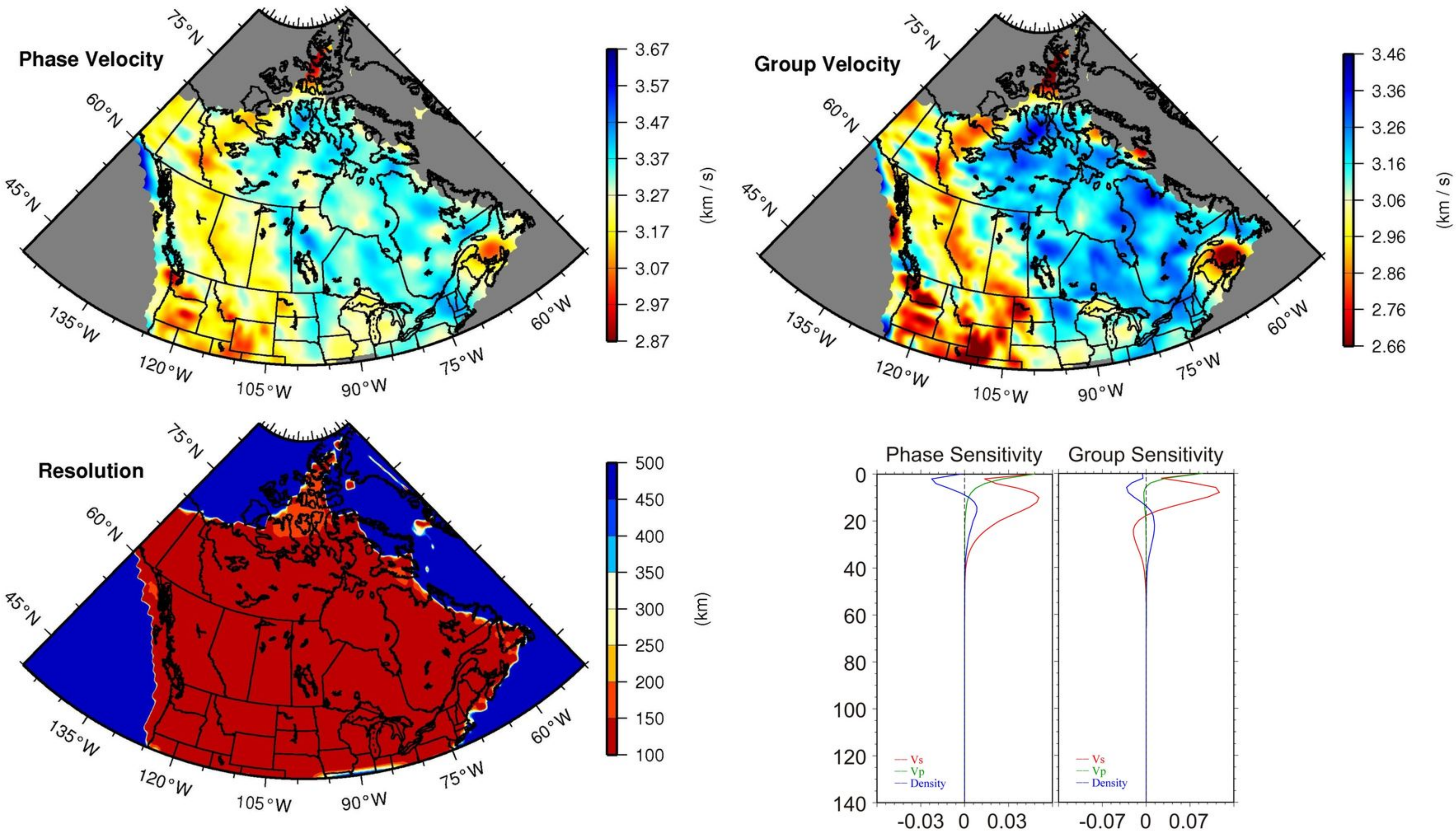

Phase Velocity
Group Velocity
Resolution
75°N
60°N
45°N
135°W
120°W
105°W
90°W
75°W
60°W
3.67
3.57
3.47
3.37
3.27
3.17
3.07
2.97
2.87
(km / s)
3.46
3.36
3.26
3.16
3.06
2.96
2.86
2.76
2.66
500
450
400
350
300
250
200
150
100
(km)
Phase Sensitivity
Group Sensitivity
0
20
40
60
80
100
120
140
-0.03
0.03
-0.07
0.07
Vs
Vp
Density

(b) Period = 35 s

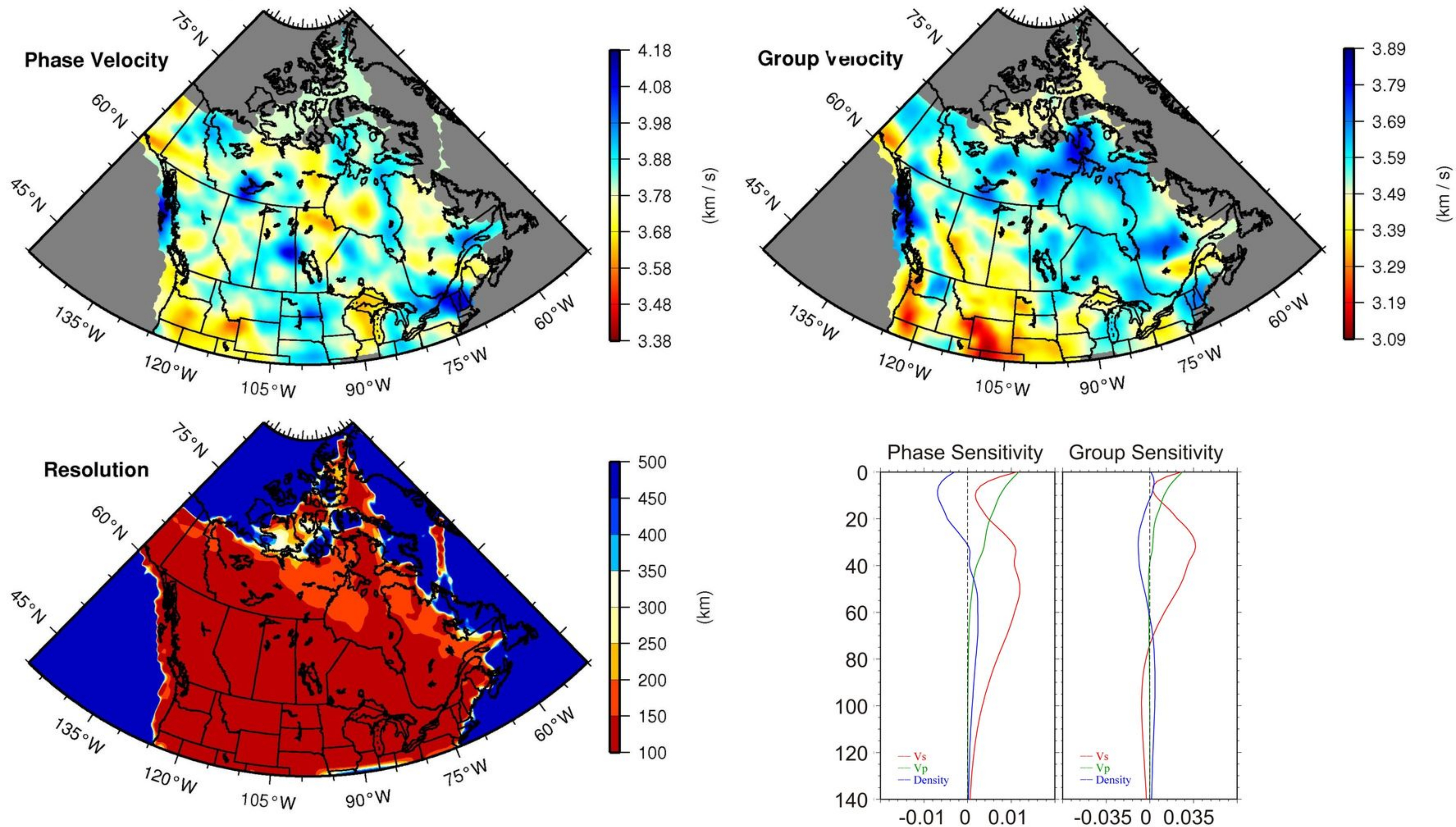
Phase Velocity
75°N
60°N
45°N
135°W
120°W
105°W
90°W
75°W
60°W
4.18
4.08
3.98
3.88
3.78
3.68
3.58
3.48
3.38
(km / s)
Group Velocity
3.89
3.79
3.69
3.59
3.49
3.39
3.29
3.19
3.09
(km / s)
Resolution
500
450
400
350
300
250
200
150
100
(km)
Phase Sensitivity
Group Sensitivity
0
20
40
60
80
100
120
140
-0.01
0
0.01
-0.035
0
0.035
Vs
Vp
Density

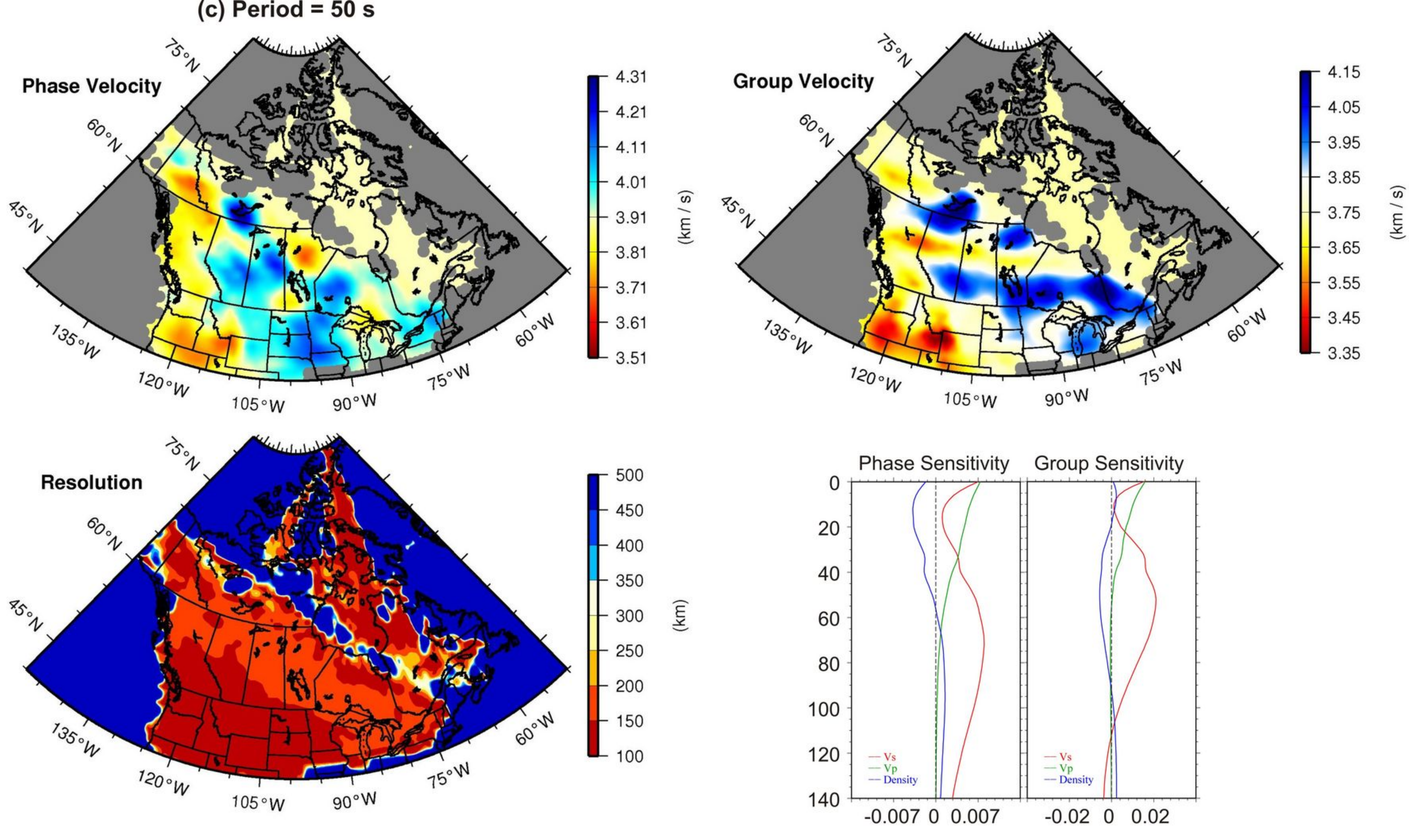

(c) Period = 50 s
Phase Velocity
Group Velocity
Resolution
(km / s)
(km)
75°N
60°N
45°N
135°W
120°W
105°W
90°W
75°W
60°W
4.31
4.21
4.11
4.01
3.91
3.81
3.71
3.61
3.51
4.15
4.05
3.95
3.85
3.75
3.65
3.55
3.45
3.35
500
450
400
350
300
250
200
150
100
Phase Sensitivity
Group Sensitivity
Vs
Vp
Density
-0.007
0
0.007
-0.02
0.02

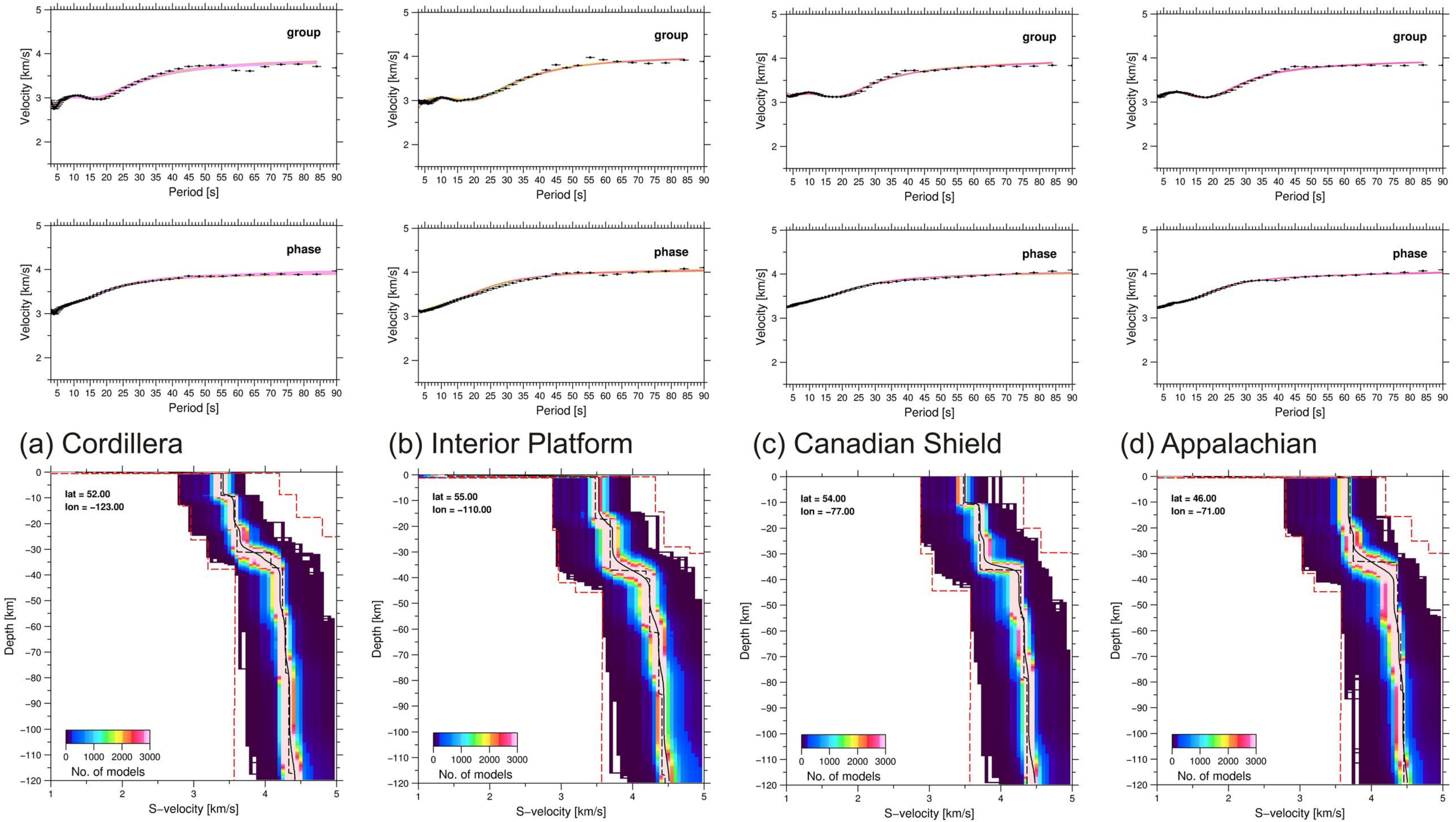
group
phase
Velocity [km/s]
Period [s]
(a) Cordillera
(b) Interior Platform
(c) Canadian Shield
(d) Appalachian
lat = 52.00
lon = −123.00
lat = 55.00
lon = −110.00
lat = 54.00
lon = −77.00
lat = 46.00
lon = −71.00
Depth [km]
S−velocity [km/s]
No. of models
0 1000 2000 3000

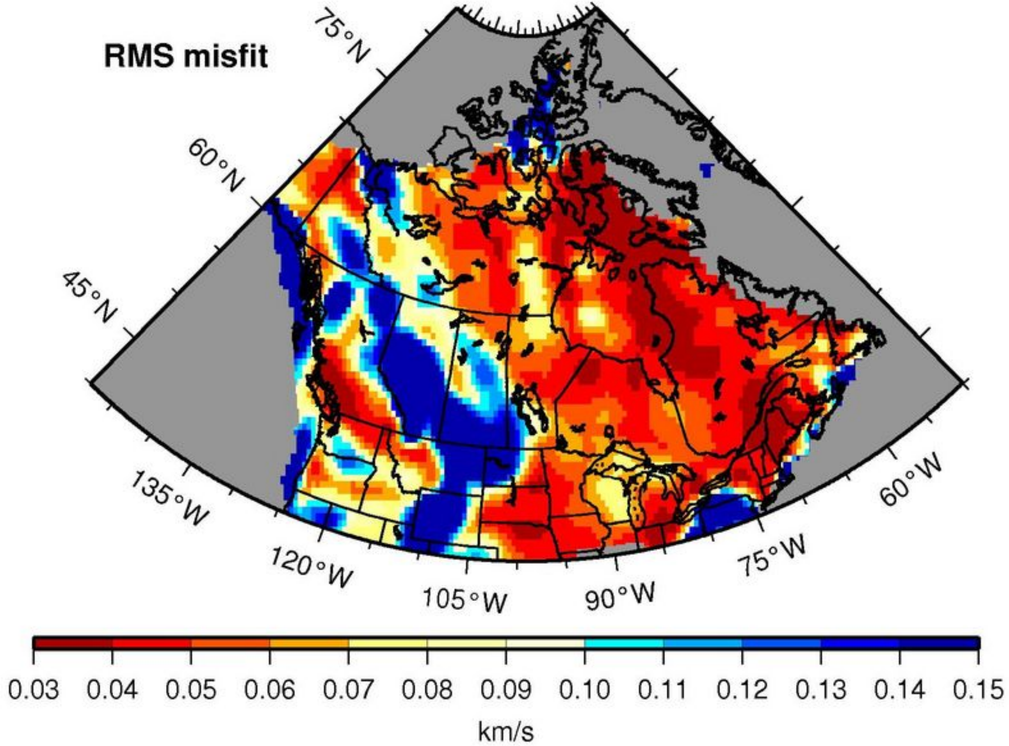
RMS misfit
75°N
60°N
45°N
135°W
120°W
105°W
90°W
75°W
60°W
0.03
0.04
0.05
0.06
0.07
0.08
0.09
0.10
0.11
0.12
0.13
0.14
0.15
km/s

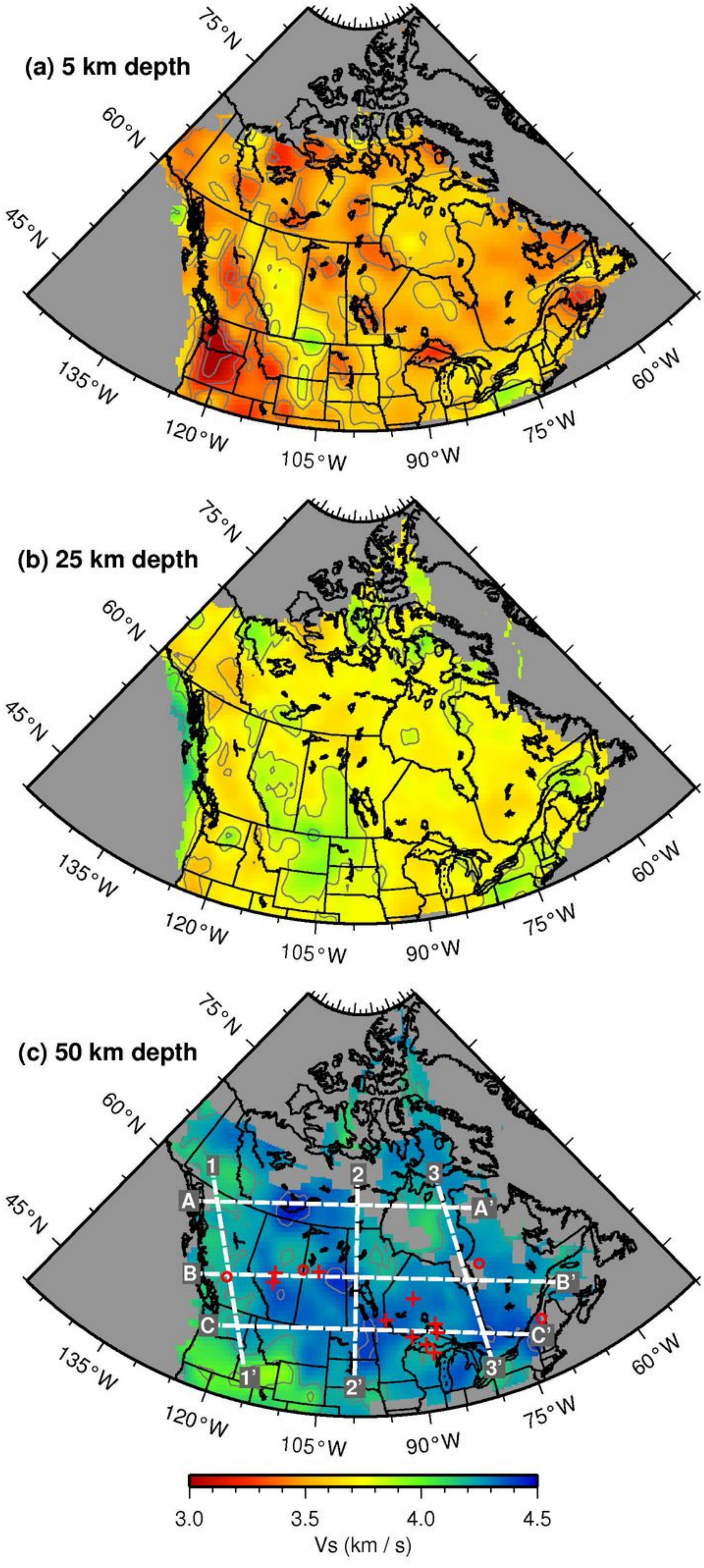
(a) 5 km depth
(b) 25 km depth
(c) 50 km depth
75°N
60°N
45°N
135°W
120°W
105°W
90°W
75°W
60°W
1
2
3
A
A'
B
B'
C
C'
1'
2'
3'
3.0
3.5
4.0
4.5
Vs (km / s)

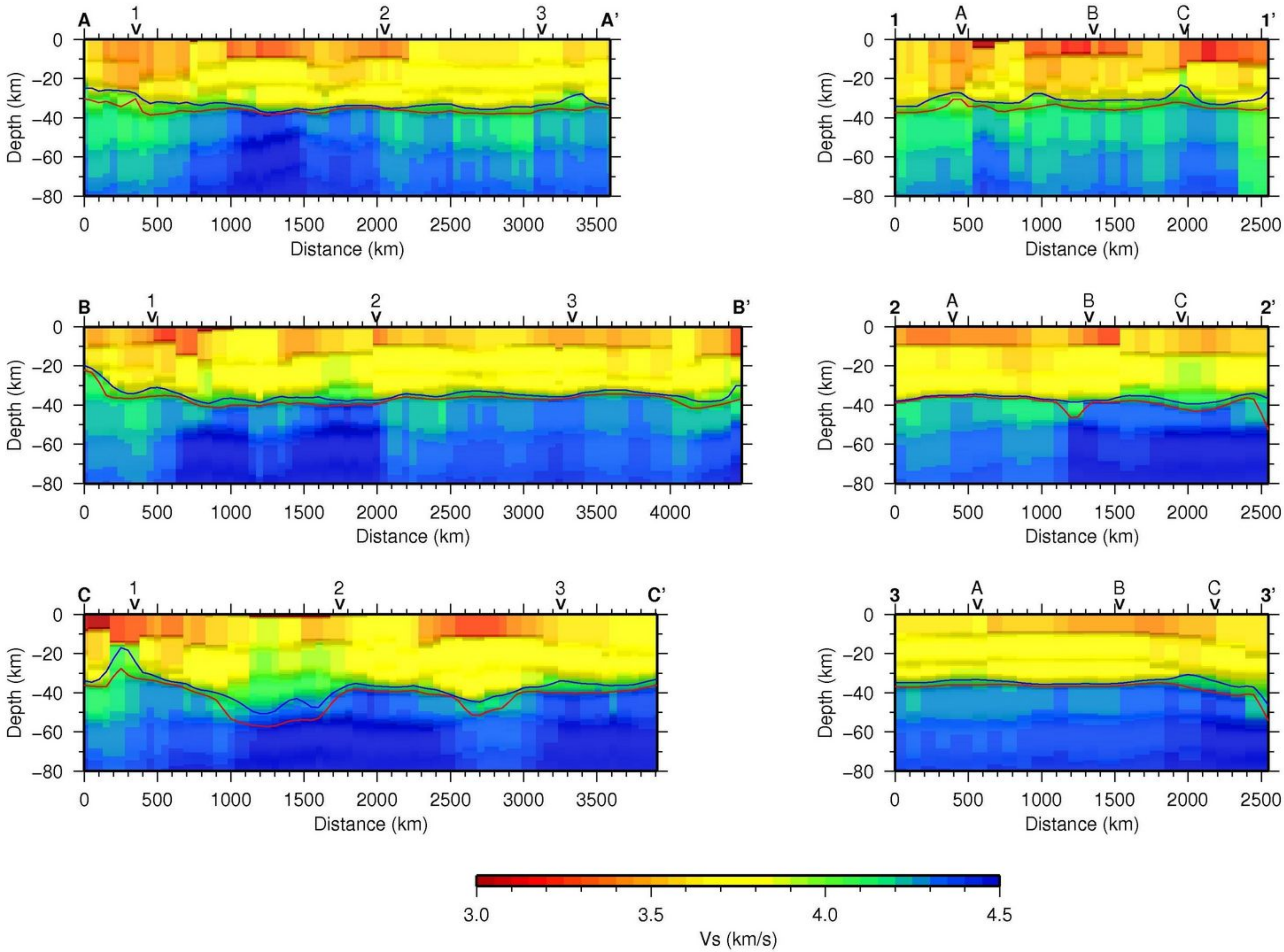

A
A'
1
2
3
Depth (km)
Distance (km)
1
1'
A
B
C
B
B'
2
2'
C
C'
3
3'
Vs (km/s)
3.0
3.5
4.0
4.5

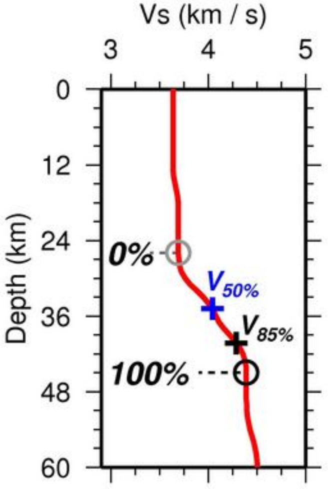
Vs (km / s)
3
4
5
0
12
24
36
48
60
Depth (km)
0%
V50%
V85%
100%

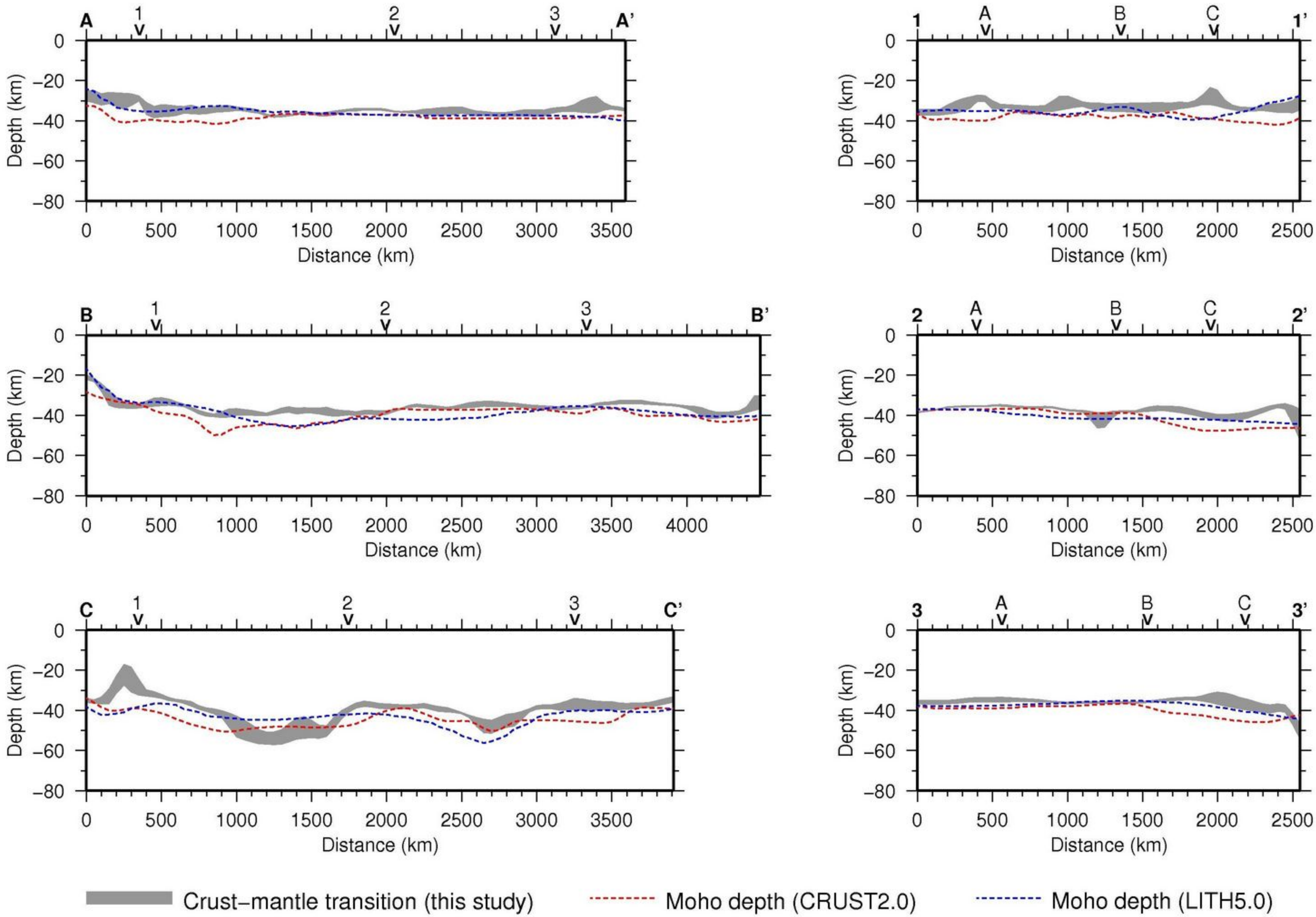

A
1
2
3
A'
1
A
B
C
1'
B
1
2
3
B'
2
A
B
C
2'
C
1
2
3
C'
3
A
B
C
3'
Depth (km)
Distance (km)
Crust−mantle transition (this study)
Moho depth (CRUST2.0)
Moho depth (LITH5.0)

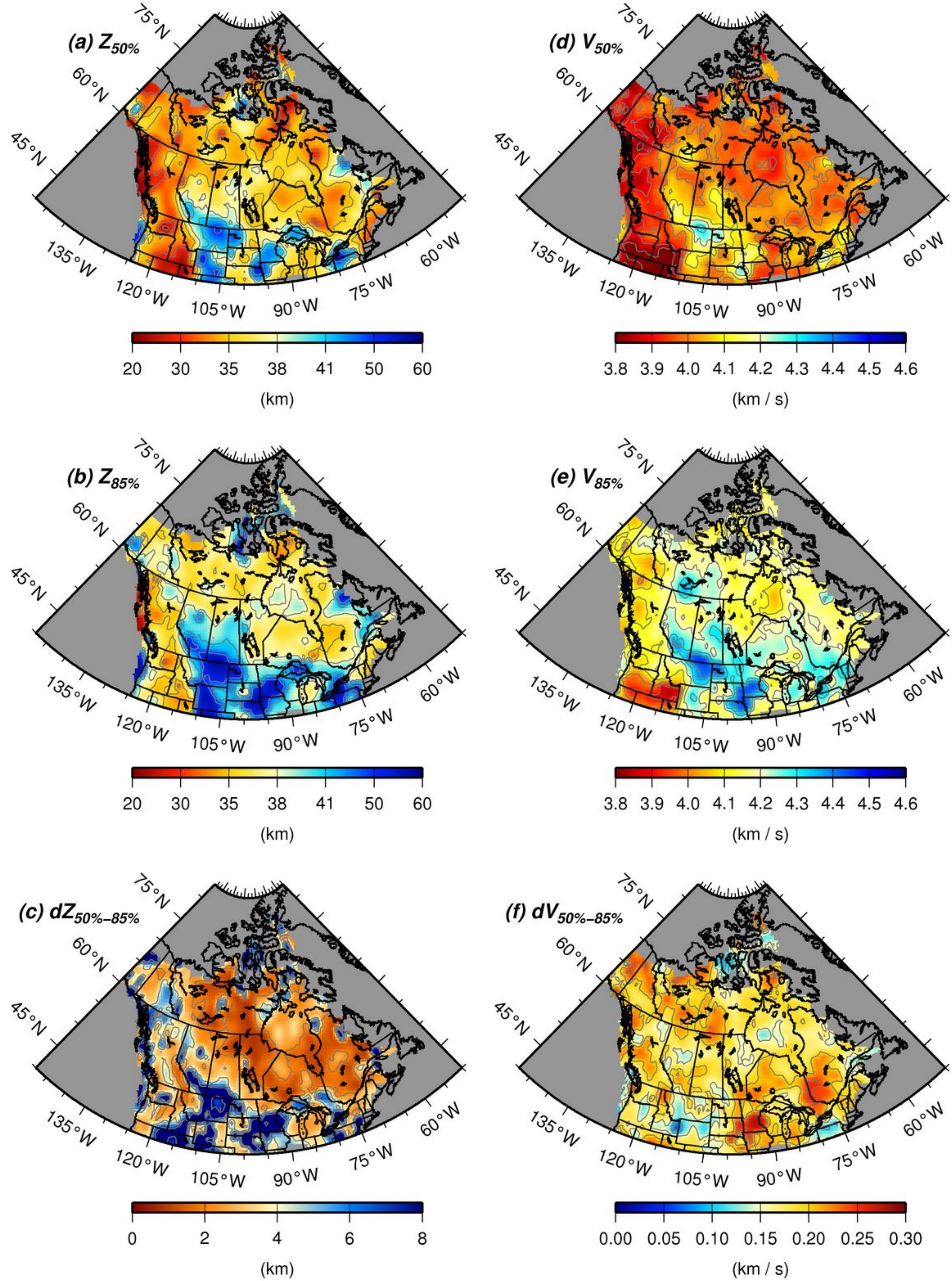

(a) $Z_{50\%}$
(b) $Z_{85\%}$
(c) $dZ_{50\%-85\%}$
(d) $V_{50\%}$
(e) $V_{85\%}$
(f) $dV_{50\%-85\%}$
75°N
60°N
45°N
135°W
120°W
105°W
90°W
75°W
60°W
20 30 35 38 41 50 60
(km)
3.8 3.9 4.0 4.1 4.2 4.3 4.4 4.5 4.6
(km / s)
0 2 4 6 8
(km)
0.00 0.05 0.10 0.15 0.20 0.25 0.30
(km / s)

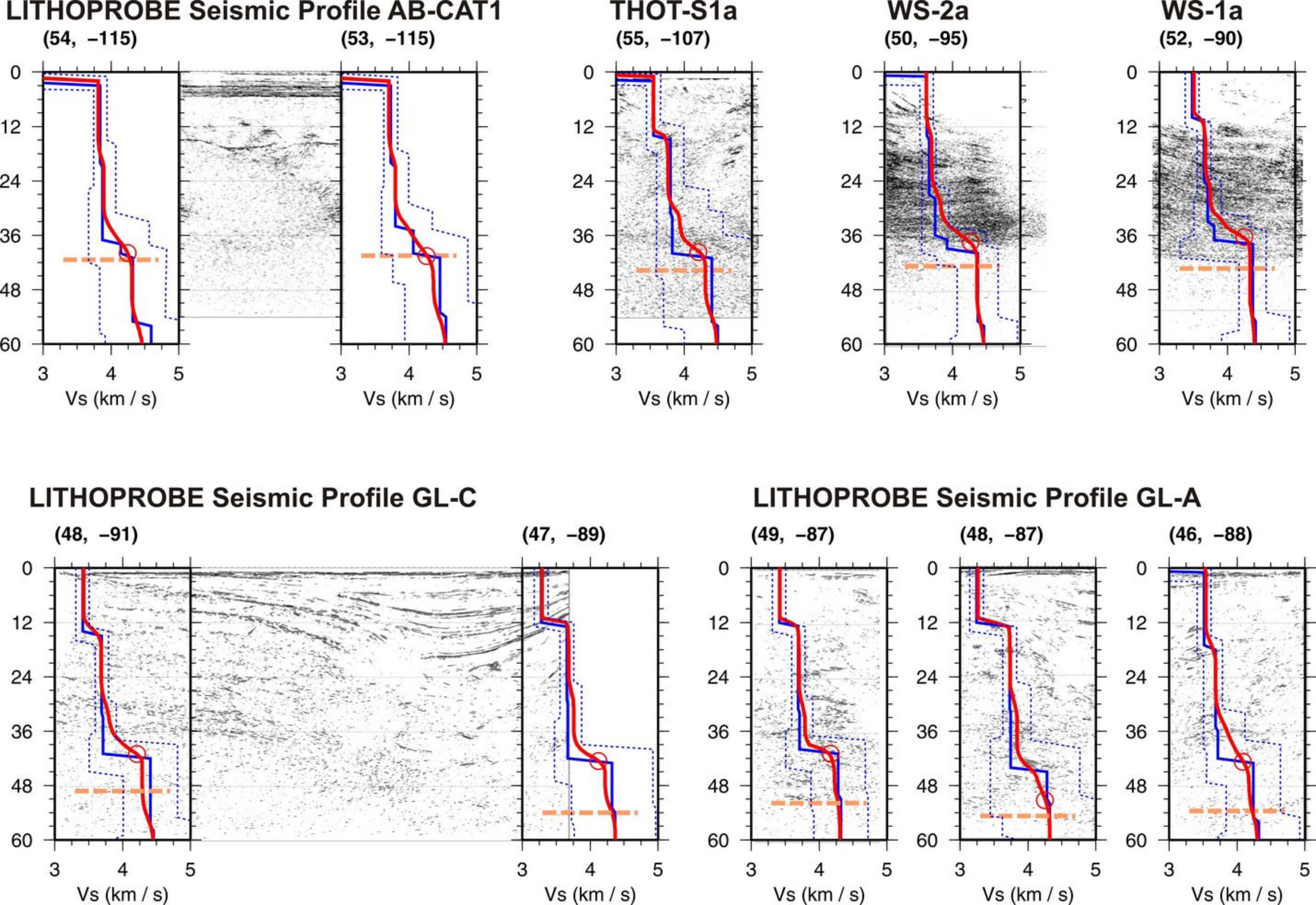
LITHOPROBE Seismic Profile AB-CAT1
(54, −115)
(53, −115)
THOT-S1a
(55, −107)
WS-2a
(50, −95)
WS-1a
(52, −90)
Vs (km / s)
LITHOPROBE Seismic Profile GL-C
(48, −91)
(47, −89)
LITHOPROBE Seismic Profile GL-A
(49, −87)
(48, −87)
(46, −88)
0
12
24
36
48
60
3
4
5

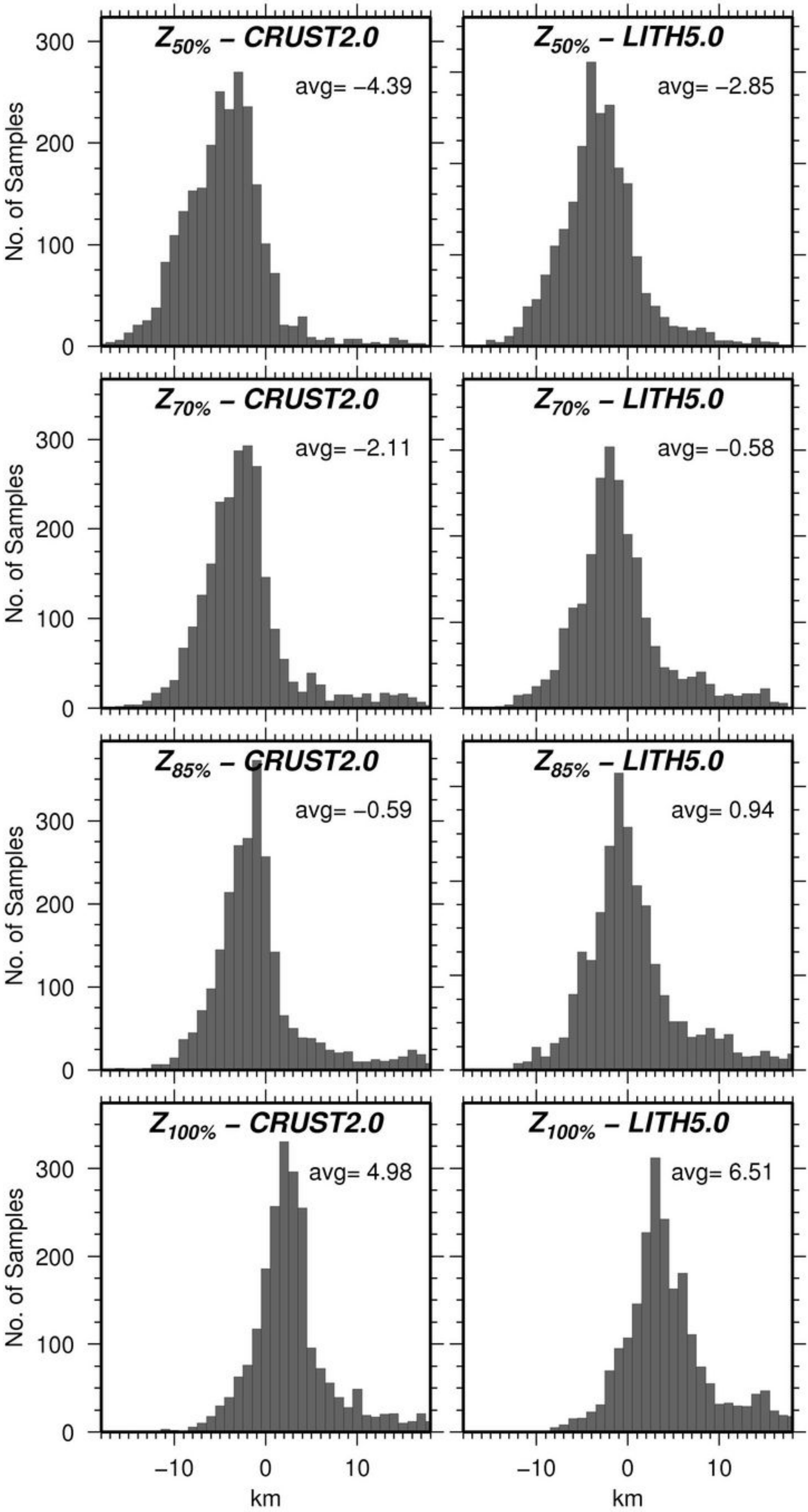

Z50% – CRUST2.0
avg= –4.39
Z50% – LITH5.0
avg= –2.85
Z70% – CRUST2.0
avg= –2.11
Z70% – LITH5.0
avg= –0.58
Z85% – CRUST2.0
avg= –0.59
Z85% – LITH5.0
avg= 0.94
Z100% – CRUST2.0
avg= 4.98
Z100% – LITH5.0
avg= 6.51
No. of Samples
km

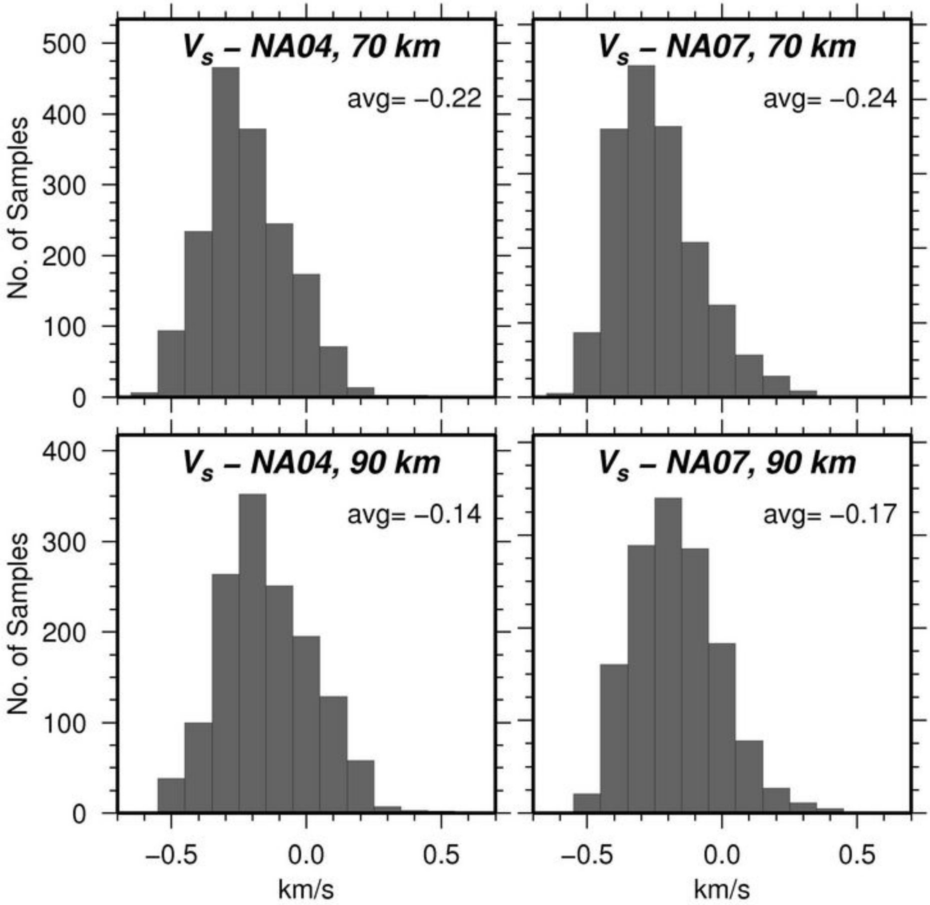
V_s – NA04, 70 km
avg= −0.22
V_s – NA07, 70 km
avg= −0.24
V_s – NA04, 90 km
avg= −0.14
V_s – NA07, 90 km
avg= −0.17
No. of Samples
km/s
0
100
200
300
400
500
−0.5
0.0
0.5